



**AFRL-RX-WP-TP-2010-4157**

# **DIGITAL REPRESENTATION OF MATERIALS GRAIN STRUCTURE (PREPRINT)**

**Michael A. Groeber**

**The Ohio State University**

**JANUARY 2010**

**Approved for public release; distribution unlimited.**

*See additional restrictions described on inside pages*

**STINFO COPY**

**AIR FORCE RESEARCH LABORATORY  
MATERIALS AND MANUFACTURING DIRECTORATE  
WRIGHT-PATTERSON AIR FORCE BASE, OH 45433-7750  
AIR FORCE MATERIEL COMMAND  
UNITED STATES AIR FORCE**

<b>REPORT DOCUMENTATION PAGE</b>				<i>Form Approved</i> OMB No. 0704-0188	
The public reporting burden for this collection of information is estimated to average 1 hour per response, including the time for reviewing instructions, searching existing data sources, gathering and maintaining the data needed, and completing and reviewing the collection of information. Send comments regarding this burden estimate or any other aspect of this collection of information, including suggestions for reducing this burden, to Department of Defense, Washington Headquarters Services, Directorate for Information Operations and Reports (0704-0188), 1215 Jefferson Davis Highway, Suite 1204, Arlington, VA 22202-4302. Respondents should be aware that notwithstanding any other provision of law, no person shall be subject to any penalty for failing to comply with a collection of information if it does not display a currently valid OMB control number. <b>PLEASE DO NOT RETURN YOUR FORM TO THE ABOVE ADDRESS.</b>					
<b>1. REPORT DATE (DD-MM-YY)</b> January 2010		<b>2. REPORT TYPE</b> Technical Paper Preprint		<b>3. DATES COVERED (From - To)</b> 01 January 2010 – 01 January 2010	
<b>4. TITLE AND SUBTITLE</b> DIGITAL REPRESENTATION OF MATERIALS GRAIN STRUCTURE (PREPRINT)				<b>5a. CONTRACT NUMBER</b> In-house	
				<b>5b. GRANT NUMBER</b>	
				<b>5c. PROGRAM ELEMENT NUMBER</b> 62102F	
<b>6. AUTHOR(S)</b> Michael A. Groeber				<b>5d. PROJECT NUMBER</b> 4347	
				<b>5e. TASK NUMBER</b> RG	
				<b>5f. WORK UNIT NUMBER</b> M02R1000	
<b>7. PERFORMING ORGANIZATION NAME(S) AND ADDRESS(ES)</b> The Ohio State University				<b>8. PERFORMING ORGANIZATION REPORT NUMBER</b> AFRL-RX-WP-TP-2010-4157	
<b>9. SPONSORING/MONITORING AGENCY NAME(S) AND ADDRESS(ES)</b> Air Force Research Laboratory Materials and Manufacturing Directorate Wright-Patterson Air Force Base, OH 45433-7750 Air Force Materiel Command United States Air Force				<b>10. SPONSORING/MONITORING AGENCY ACRONYM(S)</b> AFRL/RXLMD	
				<b>11. SPONSORING/MONITORING AGENCY REPORT NUMBER(S)</b> AFRL-RX-WP-TP-2010-4157	
<b>12. DISTRIBUTION/AVAILABILITY STATEMENT</b> Approved for public release; distribution unlimited.					
<b>13. SUPPLEMENTARY NOTES</b> Technical paper submitted to Computational Methods for Microstructure--Property Prediction. PAO Case Number: 88ABW-2009-3267; Clearance Date: 17 Jul 2009.  This work was funded in whole or in part by the Department of the Air Force. The U.S. Government has for itself and others acting on its behalf an unlimited, paid-up, nonexclusive, irrevocable worldwide license to use, modify, reproduce, release, perform, display, or disclose the work by or on behalf of the U.S. Government. Paper contains color.					
<b>14. ABSTRACT</b> Recent initiatives to accelerate the insertion of materials and link the materials design and systems design processes have called for the advancement of microstructure-property relationships. In order to achieve these goals, the development of digital microstructure models in conjunction with computational methods for simulating material response is a necessity. There have been significant advancements in the collection and representation of microstructure, which coupled with computational power increases, has yielded microstructure models with increasing complexity and accuracy. It is the emphasis of this chapter to discuss the state-of-the-art methods and current limitations in the field of microstructure representation. Specific focus will be paid to the areas of: experimental data collection, feature identification, mesh generation, quantitative characterization and synthetic structure generation. In presenting the status of the field, the key links to other fields that must be developed will also be addressed wherever possible.					
<b>15. SUBJECT TERMS</b> microstructure property relationships, computational, mesh generation					
<b>16. SECURITY CLASSIFICATION OF:</b>			<b>17. LIMITATION OF ABSTRACT:</b> SAR	<b>18. NUMBER OF PAGES</b> 58	<b>19a. NAME OF RESPONSIBLE PERSON (Monitor)</b> Christopher Woodward <b>19b. TELEPHONE NUMBER (Include Area Code)</b> N/A
<b>a. REPORT</b> Unclassified	<b>b. ABSTRACT</b> Unclassified	<b>c. THIS PAGE</b> Unclassified			

# **Digital Representation of Materials Grain Structure**

**Michael A. Groeber**

## **Abstract**

Recent initiatives to accelerate the insertion of materials and link the materials design and systems design processes have called for the advancement of microstructure-property relationships. In order to achieve these goals, the development of digital microstructure models in conjunction with computational methods for simulating material response is a necessity. There have been significant advancements in the collection and representation of microstructure, which coupled with computational power increases, has yielded microstructure models with increasing complexity and accuracy. It is the emphasis of this chapter to discuss the state-of-the-art methods and current limitations in the field of microstructure representation. Specific focus will be paid to the areas of: experimental data collection, feature identification, mesh generation, quantitative characterization and synthetic structure generation. In presenting the status of the field, the key links to other fields that must be developed will also be addressed wherever possible.

## **3.1 Introduction**

This book is motivated by the practical assessment that many questions remain to be answered regarding the effect of microstructure on materials response. Attempts to answer these questions have produced microstructure-property relationships with varying levels of detail and empiricism. The empiricism of such relationships has limited the integration of materials design in the systems design process. Instead, the systems design community tends to use databases developed through extensive experimental testing to select existing materials with a set of required performance properties. The last chapter of this book outlines the prospect of designing new materials to a desired set of properties and doing so in an accelerated fashion. One factor limiting the advancement of microstructure-property re-

relationships to allow for accelerated materials design is the disjointed treatment of microstructure by the systems design, materials processing and materials development communities. The current “industry standard” in the systems design community is to treat microstructure as a set of notes or ASTM specifications on a part drawing. As a result, the processing community uses these notes/specifications as guidelines and quality control metrics when producing materials. This approach to microstructure description is inconsistent with that used in most computational microstructure-property models. This chapter attempts to address these inconsistencies in microstructure description and outline a process for digital representation of microstructure, which allows for the more accurate inclusion of microstructure in property models.

It has become common practice to generate microstructure models for property prediction simulations with limited amounts of microstructural information included. Typically, simple geometric shapes or tessellations are used to represent microstructural features with little attention paid to accuracy beyond average values. Often though, the use of simple average quantities such as ‘grain size’ is likely to be inadequate in some microstructure-property relationships; instead one may need to consider the possibility that the full three-dimensional (3D) microstructure is important. The complexity and interplay of features in the 3D structure dictates that calculations by hand are generally impractical. Fortunately, computational power has provided a new pathway for the materials scientist to investigate microstructure-property relationships through microstructure modeling. However, computational modeling of materials requires the ability to generate digital microstructures in which the most relevant features are sufficiently described. There are multiple ways to tackle the challenge of generating 3D digital representations of microstructure. The obvious approach is to explicitly represent structure by collecting sample volumes of microstructure experimentally, whether it involves reconstructing direct images from serial sectioning or by reconstructing diffraction information from various 3D tomography techniques. A second, less direct approach is to represent structure statistically by developing tools to generate synthetic structures with statistics equivalent to some desired set, likely obtained from some experimental observation technique(s). Both of these approaches will be discussed in detail in this chapter.

With regard to the explicit representation of structure, this chapter focuses on the specific topics of experimental interrogation techniques, data processing, and mesh generation. Experimental techniques to characterize microstructure in 3D have undergone dramatic improvements in the past decade, and there now exists a host of methodologies that are capable of collecting 3D microstructural information that range from counting individual atoms (nms) to imaging macro-scale volumes (mms). However, it is important to note that there are still gaps that exist in structure collection; for example, dislocation structures cannot be readily imaged in 3D. The state-of-the-art for this field has been reviewed recently in a View-

point Set for Scripta Materialia (Spanos 2006) and thus will not be presented here. Currently there are two main experimental interrogation pathways to collect information about microstructural features in 3D. Serial sectioning experiments are more commonplace but consume the sample as part of the experiment, while x-ray methods are non-destructive but typically require the use of high-intensity x-ray sources. For the x-ray methods, there are a handful of groups world-wide that are working towards spatially-resolved crystallographic analysis of grain structures in 3D using high-intensity X-ray systems (Schmidt et al. 2004, Lauridsen et al. 2006, Budai et al. 2004, 2008, Suter et al. 2007). These methods have a significant advantage in that the sample remains intact after analysis, allowing for the possibility of time-dependent studies of microstructural changes due to thermal or mechanical input. Nonetheless, these experiments require the high brilliance of a synchrotron source that puts significant restrictions on the general applicability of the methods. Therefore, this chapter will skew its focus towards the processing and analysis of grain-level data using more universally-accessible serial sectioning experiments. Electron backscattered diffraction (EBSD) maps are often coupled with the sectioning process as an integral component of the characterization method. The incorporation of crystallographic maps enables a straightforward approach to define and segment the individual grains or precipitates that compose aggregate assemblies, and also allow for orientation-based data analysis. Most of the data-processing steps presented here are tailored for the EBSD-based section data, but all are generic in their end goal of reconstructing and segmenting features with limited experimental artifacts. Lastly, the reconstructed and processed data must be translated into a meshed structure for simulation. Various methods for surface representation and mesh generation will be presented with focus paid to the complexity, quality and physical accuracy of their resultant meshes.

The quantification of microstructure and generation of equivalent synthetic structures will be discussed in the context of the statistical representation of materials structure. The motivation for such an approach is the ability to generate many different representative microstructures that match statistically the measurements on the material of interest to a pre-determined degree of accuracy. The ability to generate synthetic structures is meant to limit the need for abundant data collection as well as supplement when direct 3D information is unavailable. The experimental methods discussed in the section on explicit representation of structure provide direct 3D information. Three-dimensional (3D) characterization methods are then required to quantify the structure so as to serve as the input information for the synthetic structure generation process. In contrast to the use of direct 3D statistics, the prospect of inferring 3D statistical descriptors from 2D observations is also a topic of interest. These stereological approaches are necessary to develop due to the fact that 3D experimental techniques remain unavailable to a large portion of the materials community.

The development of computational materials models with specific focus on the accurate incorporation of microstructure is the ultimate goal of this chapter. Two approaches for representing structure, explicit and statistical, will be addressed. The major steps in each of these processes will be described. The explicit approach requires experimental investigation, data processing and mesh generation. The statistical approach consists of statistical quantification of experimental observations and synthetic structure generation also requiring subsequent mesh generation.

## **3.2 Challenges and Previous Work**

### ***3.2.1 Characterization***

Characterizing microstructure has been classically limited to two dimensional (2D) measurements and simplistic extrapolations to three dimensions (3D). Many microstructural features can be estimated with reasonable accuracy in this manner, but arguably far more are inaccurate, if calculable at all. Limitations in these techniques have fueled a drive towards direct 3D data collection. Early attempts to collect direct 3D data [refs] were somewhat successful, but only recently have experimental and computational tools advanced to make 3D data collection readily feasible. Additionally, many of the early 3D experiments provided only visualizations and not quantitative microstructural descriptors. Equally important in the collection of microstructure are the current limits on the automation of microstructure feature identification and segmentation. Direct 3D data has proven to be exhaustive and tedious to reconstruct and segment, which has greatly hindered its applicability. Even 2D measurements have been slowed by the common inability to distinguish features of microstructure. Some microstructures display the ability to easily segment features using only either optical or Scanning Electron Microscope (SEM) imaging, but this is not always the case, especially as microstructures grow in complexity. The development of Orientation Imaging Microscopy (OIM) via electron back-scatter diffraction (EBSD) has cleared a path to automated segmentation of grains and phases over restricted scales, but does increase data collection times. Lastly, and arguably most important, the quantitative description of microstructure has been left incomplete and inconsistent. Often only average values are measured neglecting the distributions of features, leaving the microstructure incompletely described. The distributions of parameters are certainly more arduous to measure and this is usually the cause for their absence in many characterizations. However, recent developments in data collection and feature identification have allowed for these measurements to be made relatively

easily for many microstructures. Additionally, parameters are generally measured independently, resulting in the inability to correlate relationships between parameters. This is a major concern when representing microstructure, because correlations may describe the tendency of features to cluster, which may have significant effects on properties. Inconsistencies in microstructure description may arise due to a number of descriptors that quantify the same microstructural feature or parameter, but vary in their meanings and dimensionalities (for example mean linear intercept, equivalent sphere diameter, true grain volume and mean width). The various descriptors, when scaled to be comparable, can deviate significantly, causing confusion in which to use.

### **3.2.2 Modeling**

The representation of microstructure has traditionally been significantly limited by computational power, which has led to the common practice of grossly simplifying microstructure in many computational models. It is quite a standard approach to represent microstructural features as simple geometrical shapes, often with no size distribution, because “size” is rarely a part of model physics. Even in cases where attempts are made to match quantified microstructural parameters; there are generally not more than one or two parameters represented and rarely a correlation between multiple parameters. For some properties (i.e. texture or yield stress), it is possible that detailed morphological structure is unnecessary. However, other properties (i.e. fracture or strain hardening) are likely to require not only initial detailed structure, but evolving structure as well. The assumptions made in the representation of microstructure may significantly hinder the ability of physical models to predict material response. That is, a model which is developed from physical understanding of a process may be applied to a non-physical microstructure, and as a result the simulation is inherently constrained and biased. Further, when deviations between simulations and experiments are encountered, they become difficult to classify as errors in microstructure representation or errors in the physical model itself. The inability to decipher the cause of error forces incorporation of scaling constants and other relatively empirical factors to match results. Additionally, when explicit 3D structures are available, the inability to mesh the structures with a consistent quality has limited the ability to analyze the structures. The mesh generation issue remains a key concern for computation materials modeling. Lastly, determination of the necessary size of a simulated volume element (RVE) has become an entire area of study. The combination of detailed structure quantification, accurate digital representation, robust meshing techniques, properly developed constitutive laws and significant computational power is required to determine an RVE for a given property. Given that the RVE is likely to change for various properties and the significance of a simulation is

strongly linked to the use of an RVE, it becomes immediately clear that the aforementioned tools are key in the development of computational materials modeling.

### 3.3 Explicit Representation of Structure

The most straightforward and likely most accurate method for representation of 3D microstructure is to explicitly translate an experimentally collected volume into a computational model. The direct inclusion of experimentally obtained microstructural information requires few or even no assumptions about the microstructure itself; although, the data collection technique may require some prior knowledge of the microstructure. There are many experimental techniques that are capable of yielding information about the 3D grain structure of a material. In general, these techniques tend to fall in one of two categories: x-ray based methods and serial sectioning methods. Both of these general categories have advantages over the other, as well as inherent limitations. X-ray based techniques have the major advantage of being non-destructive, but are often limited by resolution and cost/availability. Serial sectioning, given the many tools capable of undertaking it, provides adequate resolution across a significantly wide range of length scales (i.e. 100s of nm to 10s of mm). However, the process is destructive and can be time-consuming and erratic. This chapter will only briefly mention some aspects about the collection processes themselves; rather the processing, analysis, and application of the resultant data will be the main focus. Further technical details can be found earlier in this book as well as elsewhere for the various x-ray (Schmidt et al. 2004, Lauridsen et al. 2006, Budai et al. 2004, 2008, Suter et al. 2007 and serial sectioning (Rowenhorst, Groeber, Raabe, Voorhies) techniques.

Serial sectioning experiments are comprised of two main tasks—sectioning and data collection—which are repeated until the desired volume of material has been interrogated. The sectioning process involves the removal of a known volume slice of material, usually determined primarily by the size-scale of the microstructural features that are to be examined. A typical rule-of-thumb is to acquire a *minimum* of 10 sections per average feature if feature shape is to be determined. The section thickness is often a compromise between the desire for high-fidelity data and the constraints of both personnel and instrument time to collect the data sets. After sectioning, the surface-of-interest is characterized through standard imaging methods or other mapping methods such as Electron Backscatter Diffraction (EBSD), Electron Dispersive Spectroscopy (EDS), etc. The resultant data obtained from a serial sectioning experiment is thus a series of parallel images that likely contain some alignment errors, require some form of feature segmentation, and may need some smoothing to account for the digital (or pixilated) images of the microstructure.



X-ray based experiments involve exposing the sample of interest with an incident beam of x-rays and measuring various aspects of the interaction of the x-rays with the sample. The fluorescence, absorption and diffraction scattering are examples of measurable results. The group of techniques that provide a description of the position and topology of the internal features of the sample are generally referred to as tomographic techniques. Within the broad class of tomography, there are multiple methods for obtaining contrast between the features of interest; for example, phase contrast tomography. In addition to obtaining topological/morphological information, if diffraction scattering is analyzed, the crystallographic information of the features can be measured as well. The limit on resolution and size of the data collected is closely linked to the intensity of the incident x-ray beam. The resultant data obtained from the x-ray experiment is a set of 3D positions with associated values of absorption (or other measures) and possibly coupled with crystallographic information. Similar to serial sectioning, there are usually artifacts in the x-ray data as well, many of which require filtering to allow for feature segmentation.

The important point to consider is that the data collection technique, while it may certainly dictate/demand some specific processing sub-steps, does not greatly change the major post-collection steps necessary to represent the experimental data as a 3D model of microstructure. Every 3D dataset requires a thorough application of a series of tools to align consecutive images, segment features of interest, and represent feature boundaries. Each of these major issues will be discussed with more focus towards serial section data. Figure 1 shows examples of some reconstructed 3D volumes obtained by serial sectioning.

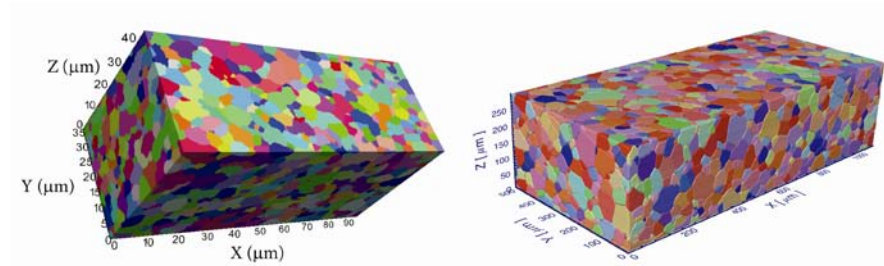


Figure 1: Sample reconstructions of (left) a nickel-base superalloy obtained through FIB-based sectioning and (right) a titanium alloy obtained by manual mechanical polishing.

### ***3.3.1 Reconstruction and Feature Identification***

#### **3.3.1.1 Image Alignment and Stacking**

It is often the case that misalignment between sections occurs during the sectioning experiment and can cause difficulties in the subsequent analysis of the dataset. These misalignments can be minimized through the use of fiducial marks coupled with manual and automated alignment tools during the data collection process, but can rarely be totally avoided. This section will address techniques used to adjust sections after the collection process has completed. First, the more general alignment solution for image data is discussed and then the more unique condition involving specialized data, such as EBSD, is presented.

The most straight-forward registration procedures involve applying simple translations to sections to improve section-to-section alignment. In the general case, this can be done with images and image processing techniques like least-square difference fitting or image convolution. In these procedures, images are translated (generally at multiples of the pixel size) in the x and y directions of the image until either a minimum difference or maximum product between pixels in consecutive images is obtained. Sub-pixel alignment can also be obtained by moving images fractions of the pixel size and interpolating the values on the new grid. Rotational alignment can also be achieved through these image processing procedures if interpolation is used to generate a grid coincident with the reference image. It should be mentioned that for these techniques to function properly, consecutive images should have consistent conditions (i.e. brightness and contrast). Often, this requirement necessitates a certain amount of image processing prior to the alignment procedures.

In many cases, the registration of separate serial sections requires more than simple translations to gain proper alignment of the image stack. This is most prevalent when combining data collected by different methods, such as micrographs from a light optical microscope and EBSD scans from a SEM, where there may be different coordinate systems, orientations, and scaling between pixels. More complex alignment procedures are also needed when the sectioning experiment lacks a fixed reference frame. If the sections are obtained by sectioning slabs through a sample rather than polishing away material, the slabs, when mounted separately, may be rotated, translated and tilted relative to one another. Alignment of these images begins by identifying a number of point features (examples would include the centers of grains, triple junctions or sample edges). One then must choose a reference frame for to which images are aligned, such as an optical image (here by noted as  $X', Y'$ ). The points ( $X, Y$ ) in a corresponding EBSD scan,

for example, should then be brought into coincidence with the optical image reference frame. The transformation from the EBSD image to the reference optical image is given by:

$$\begin{bmatrix} X' \\ Y' \\ 1 \end{bmatrix} = T \begin{bmatrix} X \\ Y \\ 1 \end{bmatrix} \quad (3.1)$$

where  $T$  is a two-dimensional transformation matrix of the form:

$$T = \begin{bmatrix} t_{11} & t_{21} & t_{31} \\ t_{12} & t_{22} & t_{32} \\ 0 & 0 & 1 \end{bmatrix}$$

For an affine transform, where image rotation and separate translations, scaling and skewing are allowed for the two directions,  $T$  is solved for all values without constraint, using the pseudo inverse matrix (a least squares fit to a system of linear equations).

However, when allowing skewing of the images, it is not possible to independently determine the rigid rotation of the two coordinate frames, which is necessary to correct the measurement of the crystallographic orientations between each EBSD section. Therefore a limited transformation matrix can be used that only allows independent scaling in the x-direction and y-direction,  $S$ , translations in the x-direction and y-direction,  $P$ , and finally an image rotation normal to the sectioning plane,  $R$ . Thus:

$$T = RPS \quad (3.2)$$

where:

$$R = \begin{bmatrix} \cos(\theta) & -\sin(\theta) & 0 \\ \sin(\theta) & \cos(\theta) & 0 \\ 0 & 0 & 1 \end{bmatrix}; P = \begin{bmatrix} 1 & 0 & P_x \\ 0 & 1 & P_y \\ 0 & 0 & 1 \end{bmatrix}; S = \begin{bmatrix} S_x & 0 & 0 \\ 0 & S_y & 0 \\ 0 & 0 & 1 \end{bmatrix}$$

The terms in the transformation matrix are then determined by a least-squares optimization. As mentioned, the decoupling of the matrix  $T$  is only required to correct crystallographic data associated with EBSD and is not necessary to do for data without such information. Further, the z-components of the matrices can be included to correct tilt errors introduced by remounting or non-parallel polishing.

As mentioned, alignment errors can be corrected in image space by processes such as least-square difference fitting, image convolutions, and Fourier transforms. However, these methods may not utilize all of the data in an image equally and image conditions can vary significantly between sections. Varying image conditions can create problems identifying features as the same feature in consecutive images. EBSD or other special data types on consecutive sections enables the use of all data points equally and generally provide a more invariant

parameter to follow between sections. The misorientation between a data point and the corresponding data point on a neighboring section can be calculated for all points in a given section. A parameter ( $\Psi$ ) can then be created to define the amount of misalignment between the two sections. The definition of  $\Psi$  is given by:

$$\Psi(k) = \sum_{j=0}^{y_{\max}} \sum_{i=0}^{x_{\max}} \Psi(i, j, k) \quad (3.3)$$

where,  $x_{\max}$  and  $y_{\max}$  are the total number of data-points in the corresponding directions and  $\Psi(i, j, k)$  is given by:

$$\Psi(i, j, k) = \begin{cases} 1 & \text{if } M[P(i, j, k), P(i, j, k-1)] \geq 5^\circ \\ 0 & \text{otherwise} \end{cases}$$

where,  $M[P(i, j, k), P(i, j, k-1)]$  is the misorientation between points  $i, j, k$  and  $i, j, k-1$ . The calculation of misorientation is discussed further in the following section on feature segmentation. The section  $k$  can be translated, by multiples of the EBSD step-size, in the  $x$  and  $y$  direction until a position with minimum  $\Psi$  is located. The parameter  $\Psi(i, j, k)$  need not be binary and can be adjusted to handle criterion tailored to other data types. Sub-pixel alignment can also be obtained using EBSD data by connecting triple points on consecutive sections and minimizing their alignment (Rollett et al. 2008).

### 3.3.1.2 Feature Segmentation and Clean-Up

Segmentation of individual features is necessary to allow for the measurement of each separately. Additionally, identifying and separating microstructural constituents provides the ability to investigate features removed from their surroundings. Grain segmentation is greatly aided by the quantitative orientation information provided by the EBSD maps, as local orientation information is the most direct means to group voxels which reduces issues of image contrast, thresholding and feature identification. There have been other, image-based techniques shown to be applicable to feature segmentation, but few have been utilized to segment features in 3D without significant user intervention (Rowenhorst, DeGraef). Feature segmentation using EBSD allows for the complete automation of the segmentation process. During segmentation, grains are identified as groups of voxels that share a similar orientation. Algorithms for identifying these groups of voxels have been presented previously (Groeber 2007, Bhandari 2007, Ghosh 2008). Commercial analysis packages (TSL, HKL) likely use a similar approach to identifying grains. The major steps of the algorithm are outlined in this section.

The initiation of each identified grain is the selection of a seed voxel. Generally, it is a useful idea to select a voxel that has been deemed to be of ‘good’ quality. Quality is defined by the EBSD data collection software and refers to the sharpness of the pattern, which is often correlated with the confidence in the assigned orientation. Usually the highest quality data tends to lie within the center of a grain, and these voxels serve as a reliable point to begin grain segmentation. A grain is then defined as the set of voxels contiguous to and with the same orientation as the seed voxel. The requirement of the voxels to have the same orientation (within a defined tolerance) is based on the fact that all regions within a grain should share a similar orientation. A list of voxels assigned to the grain is created, which initially contains only the seed voxel. The voxels that neighbor the seed voxel are checked to determine whether they have a similar orientation. The misorientation is measured to evaluate the orientation difference between the seed voxel and each of its neighbors. The value of misorientation is given by the following equation:

$$\theta = \min \left| \cos^{-1} \left( \frac{\text{tr}(O_c g_A g_B^{-1} O_c) - 1}{2} \right) \right| \quad (3.4)$$

where,  $O_c$  is the crystal symmetry operator and  $g_A$  and  $g_B$  are the rotation matrices of voxel A and B and are given by:

$$g_i = \begin{pmatrix} \cos \varphi_1 \cos \varphi_2 - \sin \varphi_1 \sin \varphi_2 \cos \Phi & \sin \varphi_1 \cos \varphi_2 + \cos \varphi_1 \sin \varphi_2 \cos \Phi & \sin \varphi_2 \sin \Phi \\ -\cos \varphi_1 \sin \varphi_2 - \sin \varphi_1 \cos \varphi_2 \cos \Phi & -\sin \varphi_1 \sin \varphi_2 + \cos \varphi_1 \cos \varphi_2 \cos \Phi & \cos \varphi_2 \sin \Phi \\ \sin \varphi_1 \sin \Phi & -\cos \varphi_1 \sin \Phi & \cos \Phi \end{pmatrix}$$

where  $(\varphi_1, \Phi, \varphi_2)$  are the Euler angles of the voxel. If the misorientation is less than the defined tolerance (i.e.  $\sim 5^\circ$ ), then that voxel is added to the list of voxels of the grain being segmented. Each voxel on the list undergoes the same process of checking its neighboring voxels until no new voxels are added to the list. After the list is complete a new seed point is generated and the voxel assignment is repeated for the next grain. An option during segmentation is to terminate the process when no unassigned voxels remain above a data quality tolerance. This ensures that no grains can be formed that include all low quality voxels. ‘Clean-up’ routines can be implemented to handle low quality points either before or after assignment. Some examples of clean-up routines will be discussed later.

The process of grouping voxels is not unique to data with orientation information. Similar algorithms can be used for image data or chemical data, where voxels of similar grayscale or chemistry are grouped together. In all three case, it may be important to consider the possibility of gradients in the data. Rarely is the interface between neighboring features perfectly sharp in the collected data. The grouping criterion may allow for additive deviation from the original seed voxel if only immediate neighbors are checked. Possible solutions include comparing the new voxel to both its immediate neighbors and the original seed voxel or compar-

ing the new voxel to an updated average value of all the previously grouped voxels.

Clean-up routines are important to handle low quality data as well as treat features that may be non-physical or difficult for the simulation tools to handle. Clean-up should ideally be performed in 3D, in order to provide the most information during the clean-up process. In any experimental technique, there will be data points that are indexed incorrectly, due either to sample preparation or collection error. These points will either be left unassigned during the feature segmentation process or they will be identified as a feature of their own. The latter case results in a large number of extremely small features that will be difficult for the simulation to handle. A minimum feature size criterion can be used to filter any extremely small features. A feature which contains less than a defined number of voxels can be dissolved and its voxels reassigned to neighboring features. The motivation to remove extremely small grains is the inability to accurately characterize features made of so few voxels and the trouble obtaining results in the simulation at those regions. The minimum size should be carefully defined and not selected arbitrarily. One important factor in selecting the minimum size is the number of voxels needed to generate a reasonable description of feature shape. Another factor in selecting the minimum size is the fraction of features that will be removed by the filter. Generally, it is undesirable to remove a large percentage of features with any one filter. If more than a few percent of the features are removed due to the minimum size criteria, it may be an indication that the resolution or quality of the data is insufficient.

Any remaining voxels, whether unassigned during or dissolved after the segmentation process, should still be assigned to neighboring features to create a fully dense structure. There are multiple options for deciding how to assign these remaining points, each of which has advantages and disadvantages. The remaining low quality points can be assigned to the feature with which they share the most surface area, to the feature which owns the highest quality neighbor of the unassigned voxel, or to the largest feature which they neighbor. In addition to the assignment of problem voxels, there are a variety of additional data processing procedures that can be applied to the 3D EBSD data, many of which are simple extensions of the 2D filters supplied in commercial EBSD analysis programs. For example, the average orientation of each grain can be calculated and assigned to all the voxels that constitute the grain. The average orientation is the orientation that minimizes the total misorientation with all the voxels in the grain. The average orientation can be solved for numerically as shown by Dawson (Dawson et al. 2001). Generally, an adequate initial estimate of the average orientation can be obtained by transforming the orientation of each voxel into a single fundamental zone and finding the center of mass of the resultant point cloud in orientation space. Additionally, the dataset can be scanned for grains that are fully contained within another grain and as a result have only one neighbor. These grains

could potentially be small subgrains that are misoriented only slightly larger than the misorientation tolerance. Datasets may also contain grains with special boundaries (i.e. twin boundaries) that can be identified and omitted from certain analyses if desired. Grains sharing these special misorientations can be merged together to leave only general grain boundaries in the dataset. These processing possibilities are provided as selected examples and not meant to comprise a full list of the options available to further process 3D EBSD data.

### ***3.3.2 Feature Surface Representation and Mesh Generation***

The following section will discuss a set of mesh generation techniques. Each technique will be critiqued with focus on its surface representation/structure, mesh quality, difficulty of implementation, inherent physicality and user bias. It is not the author's intent to identify a 'best' technique, but rather to highlight the strengths and weaknesses of each technique. All of these techniques are designed to accept as input, a discrete voxel-based structure that has been segmented and labeled as unique features. It is not necessary for the discrete data to be on a cubic grid, although the grid should be orthogonal to produce the best results in most cases. Additionally, the data need not be obtained experimentally; a synthetic structure builder can be used to generate the voxel-based structure, which will be discussed later in this chapter. Figure 2 shows a grain with different surface representations to illustrate the effect of the techniques discussed here.

#### **3.3.2.1 Voxel-Based Mesh**

Many, if not all, experimental methods collect data on a regular, discrete grid. The resultant data can then be treated as either a set of pixels in 2D or a set of voxels in 3D. Pixels and voxels provide a useful construction for automated mesh generation without the need for a separate surface representation step. The pixels or voxels can be directly imported into a Finite Element (FE) or Fast Fourier Transform (FFT) analysis code as brick elements or integration points, respectively. Another advantage of the voxel-based mesh is that the voxels (or brick elements) have good quality metrics. Two common measures of a mesh's quality are the distribution of dihedral angles of the elements and the size distribution of the elements. Voxels, even rectangular voxels, have all dihedral angles equal to  $90^\circ$ , which is nearly optimal for FE analysis. In general, all dihedral angles between  $20^\circ$  and  $160^\circ$  are acceptable for most analyses. The size distribution of a voxel-based mesh is a delta function at the grid spacing of the experimental data. Thus, there is no distribution in size of the voxels, unless some non-homogenous decimation process has been employed. With a single element size, there is no con-

cern of tiny elements much smaller than the average element size. Tiny elements are problematic when simulating the structure using FE.

However, the voxel-based mesh is not without issues to consider. Voxels create two major concerns that must be discussed to determine the suitability of this technique. First, the voxel-based construction produces a surface structure that is aliased or ‘stair-stepped’. The stepped nature of the surface is directly linked to the facts that the elements have all dihedral angles equal to  $90^\circ$  and no surface representation step is used. The edges and corners of elements on the surface create sharp discontinuities between features and can give rise to mesh instabilities. These sharp features can behave as stress concentrations during deformation simulations, leading to artificial stress and strain localizations. Second, the lack of a distribution in the size of elements often creates an abundant number of elements. If the microstructural features vary in size, it is practical to have elements that vary in size as well. Also, even if the microstructural features are of uniform size, the mesh size need not be uniform. The gradient in the property of interest can be used to grade the mesh size, where larger elements should be used where the gradient is small and smaller elements used where the gradient is large. In general, feature boundaries are areas of high gradient and the feature centers exhibit lower gradients. It is possible to decimate the voxel structure by combining neighboring voxels together in regions with small gradients in the property of interest, but not without some additional mesh compatibility steps that won’t be discussed here.

The voxel-based mesh technique is certainly the simplest to implement of the techniques to be presented here. The mesh quality is also very high. The other techniques can also produce high quality meshes, but none have the inherent quality of the voxel-based mesh. However, the voxel-based mesh has arguably the worst surface structure due mainly to its complete lack of physical meaning. The ‘stair-stepped’ structure is solely an artifact of the data collection process and not any true physical structure. The user bias is eliminated by simply using the experimental data, which at least confines the error to only the data collection itself. Due to the relative simplicity of implementation, many investigators have used the voxel-based construct for both FE and FFT simulations. Details regarding their processes and results can be found in (Lewis 2006, Deka 2004)

### **3.3.2.2 CAD-Based Surface Fitting**

The voxel structure obtained from experimental data collection can be used as input into a surface fitting algorithm. It is often practical to perform the surface fitting and subsequent surface reconstruction in a CAD environment. The goal of CAD-based surface fitting is to correct the ‘stair-stepped’ nature of the voxel structure. The process consists of identifying the set of voxels that make up the



boundary/interface between two microstructural features and fitting a polynomial or spline surface through them. After completing this step for every interface, each microstructural feature is defined as the region bounded by all of the fit surfaces corresponding to the interfaces between itself and its neighbors. The intricacies of this approach have been detailed previously (Bhandari 2007, Ghosh 2008) and are far too extensive for this chapter.

The advantage of this technique is the smooth surface representation that results from the adjustment of the polynomial surfaces or splines. However, there are difficulties encountered during the fitting and reconstruction/bounding process. First, the surfaces can be adjusted to be increasing more complex by increasing the order of the polynomial or spline. Increasing the order of the surface generally improves the fit to the voxels, but also creates issues like self intersection and local degenerate solutions. A practical limit for the surface order has been shown to be around three for a typical engineered microstructure (Bhandari 2007, Ghosh 2008). Second, creating the region bounded by a set of fit surfaces is not trivial. Each surface is fit independently and there can be incompatibilities at the areas of their intersection. Neighboring surfaces may not actually intersect or may intersect at a point significantly away from the true feature surface. This is due in large part to the lower number of data points at the edges of the surfaces. Also, data at the edges and corners of features tends to have a higher propensity for error. These issues combined with the high order fit surfaces can lead to spurious events at the areas where surfaces intersect. In addition, each feature is bounded separately and thus overlaps and gaps can be artificially created between neighboring features. These generally small artifacts are often the result of locally perturbing fit surfaces to ensure their intersection. Artifact cleaning routines can correct the overlaps and gaps by overlaying the original voxel data (Bhandari 2007, Ghosh 2008), but not without significant user intervention or advanced CAD programming.

Following the bounding of each feature and artifact correction, a volume mesh must be generated. Each surface of the bounded region can be discretized, with local curvatures of the surface dictating the local density of points on the surface. The points on the surface serve as nodes for a FE mesh. Additional nodes are required in the interior of the feature and can be positioned with various goals, such as a graded size distribution towards the center of the feature, where gradients are often lower. The volume node generation process becomes a balance between spacing nodes homogeneously to ensure the best possible dihedral angle distribution and grading the node density to yield a graded mesh structure. Once the surface and volume nodes are created, the nodes can be connected by a Delaunay triangulation process to generate a set of tetrahedrons that will be the elements for a FE analysis. The nature of the Delaunay process results in a near-optimal mesh for the given nodes. However, the tetrahedral elements generated by the Delaunay triangulation will likely still require some clean-up processes to ensure proper

element quality. In the interest of brevity, these clean-up routines will not be discussed here, but can be found elsewhere (refs).

The CAD-based technique is likely the most time intensive technique to implement. The mesh quality can be very high, provided the clean-up tools are designed properly, but it does not have the inherent quality of the voxel-based construct. The largest benefit of the CAD-based mesh is the smooth surface structure, which is arguably better than any of the other techniques. The ‘stair-stepped’ structure is generally completely eliminated. However, the process for smoothing the surfaces is not inherently physical. For example, the surface fitting criteria are generally defined to smooth while minimizing deviation from the experimental data and not to approach some physical property like minimum surface area or specified angle of surface intersection. The user bias can also be significant during the artifact correction steps, where overlaps and gaps must be assigned to neighboring features. Bhandari et al (2007) developed some physically-based tools to correct these artifacts with limited bias.

### **3.3.2.3 Direct Image-Based Meshing**

Direct image-based meshing is similar to the voxel-based approach, but with some attempt to smooth the surface structure. The central tool used in most direct image-based approaches is the marching cubes algorithm first developed by Lorenson and Cline (1987) and modified by others (refs). The marching cubes algorithm breaks a voxel-based structure into tetrahedrons based on local voxel neighborhoods. The tetrahedrons are generally high quality elements because of their tendency to be right tetrahedrons with dihedral angles of  $45^\circ$  and  $90^\circ$ . The surface structure is also generally improved over that of the voxel-based representation. The voxels on the surfaces of features are broken in a manner that removes many of the abrupt  $90^\circ$  angles that causes the ‘stair-stepped’ surface structure discussed previously.

The marching cubes algorithm creates an extremely large number of elements, because each voxel is broken into multiple tetrahedrons. The tetrahedrons tend to be close to uniform in size and thus, they are far from efficient in meshing the microstructural features. The tetrahedrons can be decimated to improve the mesh efficiency by reducing the number of elements. The decimation of the tetrahedral mesh is actually more straightforward than the decimation of the voxel-based structure directly. The surface representation, while improved, is still far from the smooth surfaces generated by the CAD-based surface fitting approach. Some commercial programs designed to generate direct image-based meshes have smoothing tools built in, but it is not known to this author what, if any, physical criteria are used. It is also possible to combine techniques by running a marching cubes algorithm on the original voxel-based structure before passing the semi-

smoothed structure on to a CAD-based approach. The semi-smooth structure is likely to improve the CAD-based approach by supplying a smoother initial surface structure, which may allow for the use of lower order fit surfaces.

The direct image-based approach has nearly the same pros and cons as the voxel-based approach, albeit the surface representation is improved. The ease of implementation, high quality metrics, and limited user bias are key advantages, but the relatively poor surface representation and the lack of physical smoothing criteria are drawbacks.

#### **3.3.2.4 Surface Area/Line Tension-Based Smoothing Methods**

The surface area/line tension smoothing technique is an attempt to combine the direct image-based method with a semi-physical smoothing process. The first step in this method is to run the marching cubes algorithm on the original voxel-based structure. After the voxel-based structure is converted into a tetrahedral mesh, a surface smoothing algorithm is applied to improve the surface representation. The difference between this smoothing algorithm and the CAD-based approach is that this algorithm has a physical driving force and the features are not treated independently. The physical driving force is related to the general belief that interfaces between features will tend to minimize their surface area in an attempt to minimize the energy of the structure. The smoothing process is presented in detail by Lee (ref) and will only be outlined here.

The smoothing process begins with the identification of all quadruple points, which are points where four features meet. Each quadruple point is connected to another quadruple point (with three of the same four features) and these connections make up the triple line network. The triple lines are not made by connecting the points directly with a line segment; they are connected by following edges of the tetrahedrons in the directions of the original voxel edges. The triple lines are initially 'jagged' from following along edges of the original voxels, but will be smoothed by balancing the minimization of both line length and deviation from the experimental data. The smoothing process involves starting at one end of the line and progressively skipping edge segments on the triple lines and monitoring the deviation of the new line from the original 'jagged' line. If a user defined tolerance is exceeded, the current segment is fixed and a new segment is initiated. The process continues until the other end of the triple line is reached. After all the triple lines have been smoothed the surfaces must also be smoothed. The surfaces are treated as a series of lines connecting triple lines across the surface. These lines are smoothed using the same process as the triple lines. The end points of all the line segments on the triple lines and surface lines are the surface nodes, similar to the nodes placed on the fit surfaces in the CAD-based method. Volume nodes

are added and connected using the same ideas discussed in the CAD-based section.

The surface area/line tension smoothing approach is an attempt to smooth the data based on physical ideas, while still being true to the experimental data. The implementation is rather simple, especially when compared to the CAD-based approach. The quality of the elements is similar to the CAD-based approach, due mainly to the similar Delaunay triangulation method for element creation used in both methods. The physically-based smoothing criterion makes for the most ‘realistic’ surface representation of the methods presented here. The user bias however, is still somewhat significant due to the user defined tolerance for deviation from the experimental data.

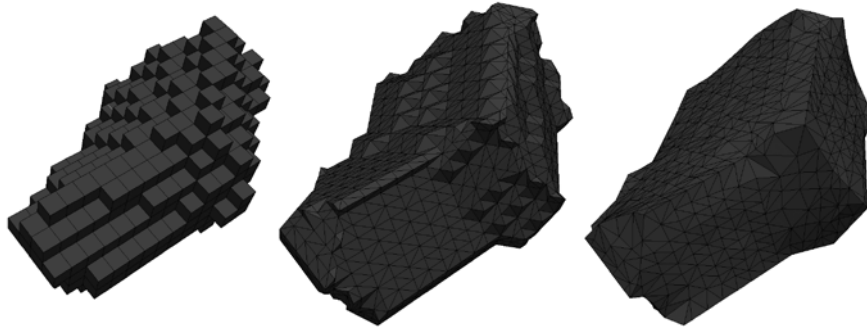


Figure 2: Surface representations of a grain using (left) voxel-based meshing, (middle) marching cubes without smoothing as commonly used in direct image-based meshing and (right) marching cubes coupled with line tension-based smoothing.

### 3.4 Statistical Representation of Structure

Representing structure in a statistical sense has multiple benefits to the computational material scientist. First, some material properties show a significant amount of scatter with the apparent cause linked to specific local feature interactions. Thus, an individual experimental volume may not accurately represent the variation in locally critical neighborhoods. Statistically-equivalent instantiations of the experimental volume may highlight the likelihood of the occurrence of such neighborhoods and permit simulation of their influence on behavior. Additionally, statistically quantifying structure can offer insight in to the representative nature of a structure in relation to a specific property of interest. That is, the convergence of a property and some set of statistical descriptors can be linked to determine a representative volume element (RVE) for that property. Further, statistical-based

structure builders can be used when the 3D structure is not available. If the 3D statistics of a structure can be inferred from 2D observations, which will be discussed later, then a 3D structure can be created where one was not available. Lastly, the statistical description of structure, if coupled with rapid and robust instantiation tools, can allow for the compression of data from large experimental datasets to a list of statistical descriptors used to generate structures when needed.

The following section will discuss the critical steps in generation of statistically-based synthetic structures, specifically statistical quantification methods, structure generation processes, and metrics for the validation of equivalence.

### ***3.4.1 Quantitative Description of Structure***

#### **3.4.1.1 Feature Size & Volume**

Feature volume can be calculated simply by summing the number of voxels that are assigned to each feature. Each voxel has an associated volume given by  $V_{\text{voxel}} = \delta \varepsilon^2$ , where  $\delta$  is the section thickness and  $\varepsilon$  is the pixel/step-size of the 2D image or EBSD map. The feature volume is calculated by  $V_{\text{grain}} = N_v \cdot V_{\text{voxel}}$ , where  $N_v$  is the number of voxels in the grain. In addition to measuring the true feature volume, the equivalent sphere radius (*ESR*) can be calculated (Groeber 2007). The distribution of *ESRs* is useful for comparison with classical descriptions of feature size (or radius/diameter), which often involved some extrapolation from 2D. Additionally, various theoretical distributions have been developed to fit the *ESR* distribution (Enomoto 2004, Feltham 1957, Hillert 1965, Louat 1974). Figure 3 shows a sample distribution of *ESR* for a nickel-base superalloy along with fit theoretical distributions.

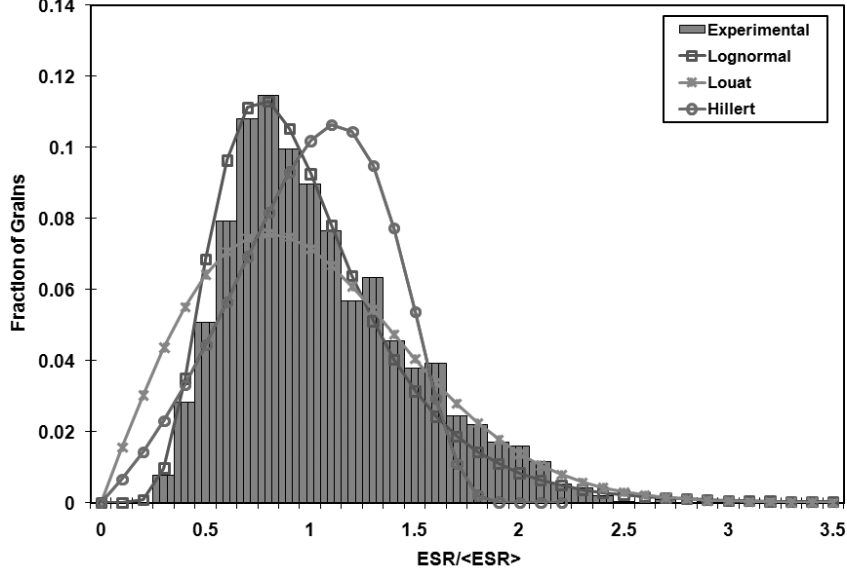


Figure 3: Plot of equivalent sphere radius ( $ESR$ ) for a nickel-base superalloy along with three fit theoretical distributions.

Another measure of feature size is the mean width of the feature. The mean width is given by:

$$L = \frac{1}{2\pi} \sum_{i=1}^v \varepsilon_i \beta_i \quad (3.5)$$

where,  $v$  is the number of edges on the feature,  $\varepsilon$  is the length of the edge and  $\beta$  is the angle between the normals of the faces that meet at the edge. Mean width is a measure of the linear dimension of a feature and was shown by Hadwiger (1957) to exhibit the property of additivity. Mean width can be calculated analytically for all flat-faced polyhedra (MacPhearson and Srolovitz 2007), which means that mean width can be easily computed for all grains after any of the surface mesh generation processes discussed previously.

### 3.4.1.2 Feature Shape

The irregular geometries that are typical of features in some materials make feature shape a difficult parameter to unambiguously describe. This is especially true due to the lack of general shape descriptors, where most descriptions of shape involve combining groups of size parameters to generate a unitless value (Russ 1983). Examples of possible shape descriptors include: length/width (aspect ratio), area/convex area (solidity) and length/fiber length (curl). A common practice

is to fit an ellipsoid (or ellipse in 2D) to the feature (Saylor 2004, Brahme 2006). A systematic method of generating ellipsoidal inclusions from voxel data obtained by serial-sectioning has also been developed (Ghosh 1999). In this method, the zeroth order moment ( $I_0$ ), first order moments ( $I_x, I_y, I_z$ ) and second order moments ( $I_{xx}, I_{yy}, I_{zz}$ ) are first calculated for each feature by adding the contribution of each voxel belonging to an identified feature. The coordinates of the centroid for the best-fit ellipsoid are computed from the zeroth and first order moments as:

$$x_c = \frac{I_x}{I_0}, \quad y_c = \frac{I_y}{I_0}, \quad z_c = \frac{I_z}{I_0} \quad (3.6)$$

Next, the principal directions, corresponding to the principal axes of the ellipsoid are calculated from the eigenvalues and eigenvectors of the second order moments  $I_{ij}$ ,  $i, j = 1, 2, 3$ . The major axis ( $2a$ ), minor axis ( $2c$ ) and intermediate axis ( $2b$ ) of the ellipsoidal grain are solved from the relations of the principal second moments of inertia as:

$$a = \left[ \frac{A^4}{B \cdot C} \right]^{\frac{1}{10}}, \quad b = \left[ \frac{B^4}{A \cdot C} \right]^{\frac{1}{10}}, \quad c = \left[ \frac{C^4}{A \cdot B} \right]^{\frac{1}{10}} \quad (3.7)$$

where,  $A, B$  and  $C$  are given by:

$$A = \left( \frac{15}{4\pi} \right) \cdot \left( \frac{I_1 + I_2 - I_3}{2} \right), \quad B = \left( \frac{15}{4\pi} \right) \cdot \left( \frac{I_1 + I_3 - I_2}{2} \right), \quad C = \left( \frac{15}{4\pi} \right) \cdot \left( \frac{I_2 + I_3 - I_1}{2} \right)$$

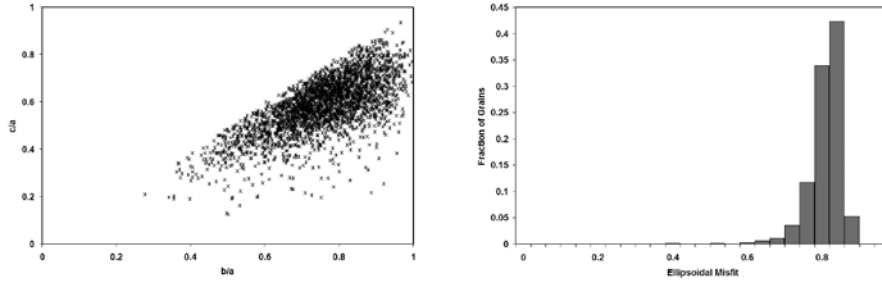


Figure 4: Plot of (left) the distribution of grain aspect ratios for a nickel-base superalloy, obtained from a best-fit ellipsoid and (right) the accuracy indicator, termed ellipsoidal misfit, that describes the closeness of the fit ellipsoids.

In some cases the ellipsoidal representation of features is an oversimplification that should be quantified. Correspondingly, an accuracy indicator of the ellipsoidal representation can be developed (Groeber 2007). The best-fit ellipsoid based on the moment analysis is scaled slightly to be of the same volume as the grain with the same aspect ratios and orientation. The fraction of the grain's voxels that lie within the best-fit ellipsoid is calculated. If the grain is perfectly ellipsoidal then the value of this quantity would be very near 1 (with the voxel size relative to the

feature size controlling the nearness to 1). Decreasing values indicate more complex and likely concave shapes that are poorly represented by an ellipsoid. Figure 4 shows a sample plot of the distribution of grain aspect ratios for a nickel-base superalloy as well as the corresponding accuracy indicator plot.

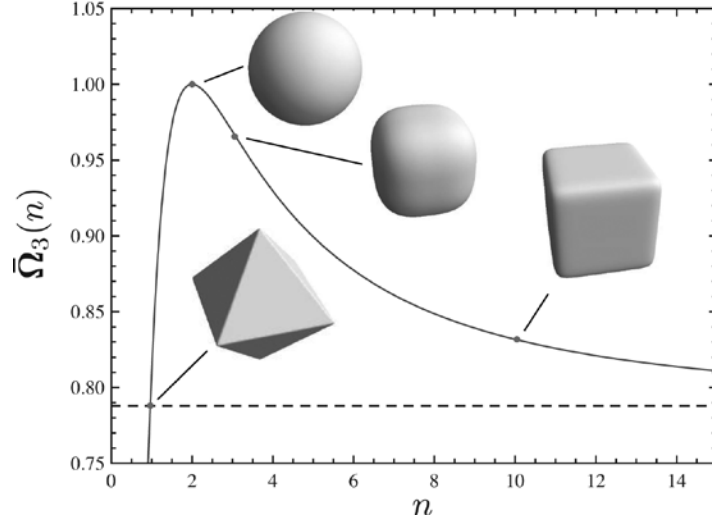


Figure 5: Plot of the relationship between  $\bar{\Omega}_3$  and  $n$ , where  $n$  is the exponent in the superellipsoid equation given by equation 8.

In the case that the ellipsoidal representation is not sufficient, higher order moments may need to be considered. However, there is more information in the second-order moments, beyond the aspect ratios, that is rarely used in microstructure description. For the second order moments, there are three moment invariants. The third moment invariant, where the first two are essentially the aspect ratios, offers more detail on the shape of a feature (MacSleyne et al 2008). While it is true that the three invariants of the second order moments are not sufficient in describing the true shape of the feature, there are techniques that can be used to incorporate all three invariants and improve on the current description of shape. For example, if a class of shapes is selected (i.e. superellipsoids or truncated octahedrons), the third moment invariant can be linked to parameters that fully define these shapes. In the case of the superellipsoid, the third invariant, known as  $\Omega_3$ , can be linked to the exponent in the equation that defines a ‘superellipsoid’ (MacSleyne et al 2008):

$$\left(\frac{x}{a}\right)^n + \left(\frac{y}{b}\right)^n + \left(\frac{z}{c}\right)^n = 1 \quad (3.8)$$

where,  $a$ ,  $b$  and  $c$  are the semi-axes of the superellipsoid. The relationship of  $\Omega_3$  to  $n$  is given by:



$$\Omega_3 = F^3[n] \quad (3.9)$$

where,

$$F[n] = 20 \frac{\Gamma\left[1 + \frac{1}{n}\right]^3 \Gamma\left[\frac{5}{n}\right]}{\Gamma\left[\frac{3}{n}\right] \Gamma\left[1 + \frac{3}{n}\right]^{\frac{5}{3}}}$$

and  $\Gamma[x]$  is the complete Gamma function. Figure 5 shows the relationship of  $\Omega_3$  and  $n$ , along with some example feature shapes for selected values of  $n$ . It becomes obvious from the plot that utilizing  $\Omega_3$  enables the description of shape variation beyond just aspect ratio changes.

### 3.4.1.3 Number of Neighbors

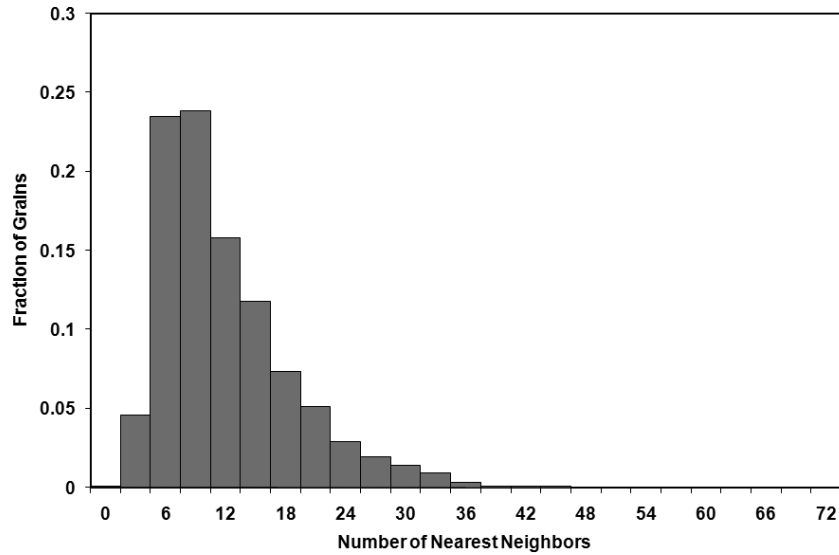


Figure 6: Plot of the distribution of the number of neighbors for grains in a nickel-base superalloy.

In addition to the shape of features, the number of nearest neighbors is another example of a parameter that cannot be determined directly from 2D measurements but is easily determined in 3D. Here, the voxels of each feature are checked to see if they neighbor another feature. If a neighboring voxel belongs to a different feature, the two features are neighbors. This process is exceedingly useful because it not only determines the number of neighbors, but it identifies the feature connec-

tivity in the structure, which allows for further automated investigation of any parameter involving neighbor interactions. Note that when checking neighboring voxels, only voxels that share a common face, not a common edge or corner, are considered. This requires the features share some actual area and avoids counting features that meet at only an edge or point. Figure 6 shows a sample plot of the number of neighbors distribution for a nickel-base superalloy.

#### 3.4.1.4 Correlations between Parameters

The correlation or mutual relationship between parameters may be important because it provides additional information regarding the morphology and spatial arrangement of features. The feature connectivity coupled with the parameters of each individual feature allows for the relationships between parameters as well as the clustering of critical features to be studied. It is desirable to quantify the degree of correlation between two selected parameters. A quantity called the correlation ratio,  $\eta^2$ , can be used for this purpose (Kenney 1947). The correlation ratio is a preferred metric in comparison to the correlation coefficient,  $r$ , because it can be used with non-linear relationships. The correlation ratio is the square of the correlation coefficient ( $r^2$ ) if the relationship is linear. If the relationship is non-linear, the magnitude of the correlation ratio is larger, but retains a value between 0 and 1. The formula for the correlation ratio is given by:

$$\eta^2 = \frac{\sum_{b=0}^{N_b} n_b (\bar{y}_b - \bar{y})^2}{\sum_{i=0}^{N_g} (y_i - \bar{y})^2} \quad (3.10)$$

where,  $N_g$  is the total number of features,  $N_b$  is the number of bins,  $n_b$  is the number of observations in a given bin  $b$  and,

$$\bar{y}_b = \frac{\sum_{i=0}^{n_b} y_{bi}}{n_b}, \quad \bar{y} = \frac{\sum_{b=0}^{N_b} n_b \bar{y}_b}{\sum_{b=0}^{N_b} n_b}$$

The correlation ratio can be thought of as the percent of the total variance of the dependent variable accounted for by the variance between groups of the independent variable. Seen in the equation is that if there is a large difference between the mean of the whole data set and the means of the individual bins, then the correlation ratio is high. Figure 7 shows a correlation plot relating feature size to a number of morphological parameters for a nickel-base superalloy. The grains of the superalloy were separated by their *ESD* and the averages of other morphological parameters were calculated for grains of similar *ESD*. The averages for each size

bin were then normalized by the average of the corresponding morphological parameter for all sizes. It becomes quite clear which parameters are strongly correlated with size when observing the trends in Fig. 7.

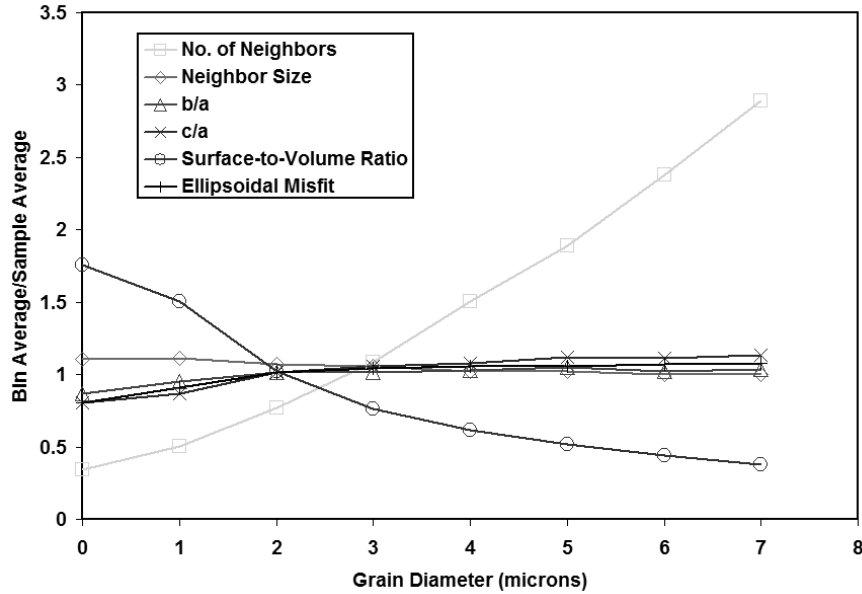


Figure 7: Plot of the correlation between grain size (i.e.  $ESD=2*ESR$ ) and other morphological parameters. Bin average refers to the average of a parameter for all grains within a given size bin and sample average refers to the average of the parameter for all grains, regardless of size bin.

### 3.4.1.5 Crystallographic Texture

Many of the traditional analysis of 3D EBSD data are directly analogous to the traditional two-dimensional counter analysis. For example the volume fraction of a particular phase and the Orientation Distribution Function (ODF), since the area fraction is exactly equal to the volume fraction for a random section through a material. However, the 3D analysis can often add inform these analysis, for example, only through a 3D analysis can the preferred morphological orientation, such as that measured by the ellipsoid of fit, be correlated with the crystallographic texture measured in the ODF.

Other measurements have 2D to 3D analogs that are related through stereological relationships that give a statistical equivalence of the properties. An example of this would be the distribution of misorientations across feature boundaries in a material. In the 2D section, one can easily measure the misorientation across the

boundary, but the line-length of a given boundary is not directly related to that boundary's area. However, if enough boundaries are collected in 2D section with a similar misorientation, one can apply the stereological relation,  $S_V = 4B_A/\pi$  where  $S_V$  is the surface area per unit volume, and  $B_A$  is the boundary length per unit area (Russ 1986). It should be noted a very large number of boundaries need to be present in the 2D section in order to obtain a statistically significant number of boundaries for each misorientation type for this analysis to be valid. In the case of a 3D reconstruction, the measurement of the misorientation distribution is relatively straightforward since, as discussed above the feature's nearest neighbor misorientations and their boundary areas can be directly calculated from the 3D reconstruction, thus the misorientation distribution function can be directly measured without assumption. Figure 8 shows a set of pole figures and the misorientation distribution for a nickel-base superalloy.

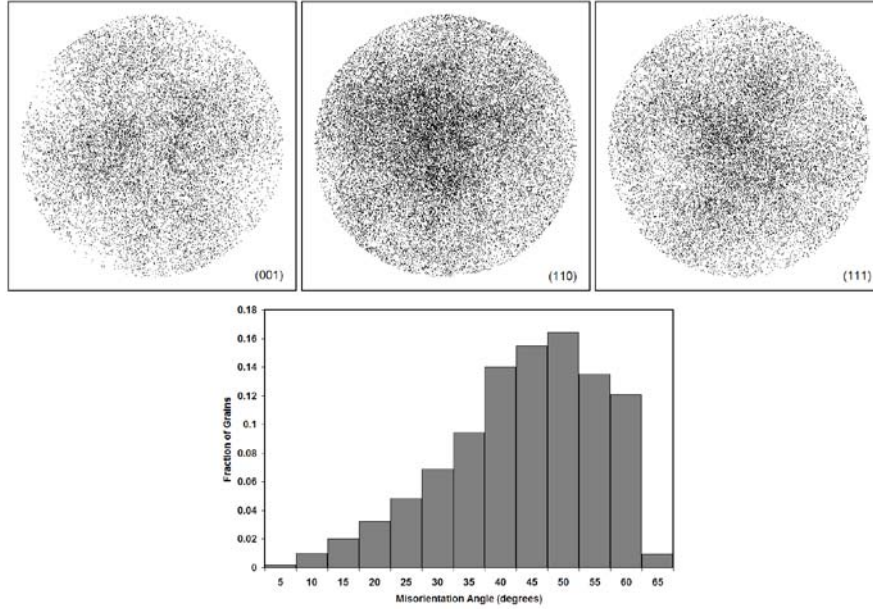


Figure 8: Plot of (top) pole figures for a nickel-base superalloy and (bottom) the misorientation distribution of the same nickel-base superalloy.

#### 3.4.1.6 Interface Character Distribution

There are many analyses that can only be measured directly through 3D reconstruction of the material. In a very general sense, these analyses can be seen as the correlation of a specific 3D geometry with the crystallographic orientation. One of the most relevant applications of this is the determination of crystallographic in-

terface orientations, which requires directly correlating the crystallographic orientation of an object with the local interface normal.

One of the most common 3D visualization techniques is to form a surface mesh of the object so that the interface of the object is described as a 3D mesh of discrete interconnected triangles. The conversion from a regularly gridded 3D array of data (such as a stack of images) is most often accomplished using a fast-marching cubes algorithm that converts the volumetric regular array data form to a surface mesh (Lorenson and Cline, 1987). Often it is necessary to apply some degree of surface smoothing in order to remove pixel-like artifacts from the surface mesh, as discussed in the section on surface representation and mesh generation. Once the surface is described in terms of a set of triangles, the properties of these triangles can be used to quantify the interfaces of the 3D reconstruction, particularly the local interface normal. The normal  $\hat{n}$  and the area  $A$  of each triangle in the surface mesh is given by:

$$\hat{n} = \frac{\vec{e}_1 \times \vec{e}_2}{|\vec{e}_1 \times \vec{e}_2|}; A = |\vec{e}_1 \times \vec{e}_2|/2 \quad (3.11)$$

where,  $\vec{e}_1$  and  $\vec{e}_2$  are the two edge vectors of the triangle.

One powerful construction that can be formed from this type of data is the Interface Normal Distribution (IND) (Kammer & Voorhees 2006). The IND is constructed by first placing the collection of all the interface normal vectors on to a unit sphere. The normals are then binned (weighted by the surface areas of the triangles) according to orientation, then normalized by a random distribution of orientations. Therefore, an orientation on the spherical histogram that has a strong intensity corresponds to a large surface area that shares that orientation. This spherical histogram is then projected to a 2D plot using a stereographic projection (typically along the +z direction, but this is a matter of how one wants to represent the data), preserving the angular relationships between the orientations in the plot producing the IND plot. It should be noted that if the binning of the data occurred on the projected data space of the stereoplot, rather than on the unit sphere, the intensities of the histogram would be altered by the nonequal-area nature of the stereographic projection. Because the binning of the data occurs on the unit sphere, this artifact is avoided and a randomly distributed shape (like a sphere) would have a flat intensity. For INDs that contain peaks, the exact shape of peaks on the stereoplot would still be slightly altered by the projection especially close to the center poles and edges of the stereoplot. The stereographic projection has extremely large distortions for orientations that have a -z component. To avoid this often it is necessary to project each hemisphere separately, however this can be avoided if there is crystallographic symmetry, which allows the plot to be compressed to a stereographic triangle.

The inclusion of the local crystallographic orientation along with the local interface normal means that the interface normals can be expressed in the crystallographic coordinate system as well, creating a Crystallographic Interface Normal Distribution (CIND). The only variation in the construction of the CIND is that before the normals are binned on the unit sphere, they are rotated to the crystallographic coordinate system using the euler angles of the object in question. There are two analyses that especially lend themselves to this type construction, the examination of individual objects and examining the overall crystal interface texture in a sample, which will be briefly reviewed.

Rowenhorst et. al. (2006) used the CIND analysis to examine the facet planes on individual coarse martensite crystals, as shown in Figure 9 (right). By identifying the peaks within the CIND, and fitting planes to the corresponding triangles the average crystallographic facet normal was determined. This article also introduced a unique visualization technique in which the interfaces in the 3D reconstruction of the martensite crystals were colored according to the local interface crystallographic normal (Fig. 9 middle). The coloring scheme is identical to that used to create an Inverse Pole Figure (IPF) but unlike the IPF, where each point in the image is colored according the crystallographic direction that points along an arbitrary section plane direction (Fig. 9 left), here the interface was colored according the crystallographic direction that is parallel with the surface normal. This visualization contains essentially the same exact information as the CIND construction with the added advantage of being able to link crystallographic orientation to specific morphological features, but unlike the CIND, the information presented is not quantitative.

Saylor et. al. (2004) significantly expanded on the CIND construction to include not only the interface distribution of grain boundaries in poly-crystalline MgO, but to include the full five parameter space of the grain boundaries, constructing the Grain Boundary Character Distribution (GBCD). By examining the full five parameter space, they were able to not only determine the interface texture for the system, but also the interface texture for particular grain misorientations. Since this initial study, the GBCD has been determined for many more materials systems including Al, Ni, Cu, Brass, and Ti-6-4 (Saylor, 2004; Randle 2008a; Randle 2004; Randle 2008b).

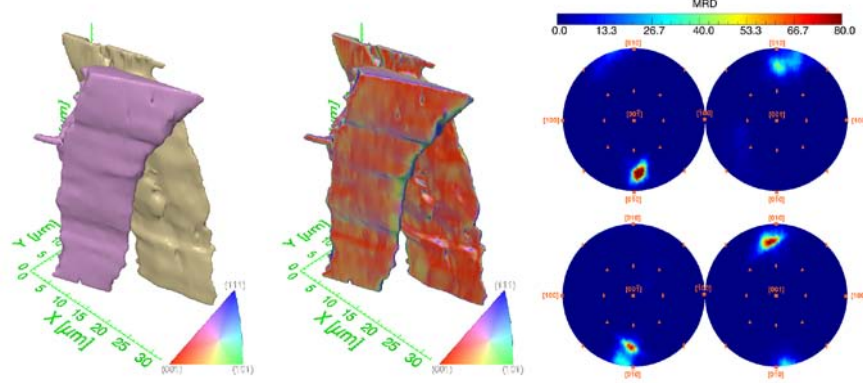


Figure 9: Reconstruction of two coarse martensite crystals in HSLA-100 steel. (left) Color indicates the crystallographic direction that is parallel with the z-axis. The difference in color indicates that the martensite crystals represent separate martensite variants. (middle) Color indicates the crystallographic orientation of the local interface normal at each local patch of the interface. Note that while the crystals represent different variants, the crystal facets have similar crystallographic normals. (right) Crystallographic Interface Normal Distribution (CIND) plots of the two martensite crystals, where the upper and lower CINDs correspond respectively to the purple and yellow crystals in the left image. The peaks in the CIND indicate the average orientation of the facet planes of the crystals; peak intensities indicate Multiples of a Random Distribution (MRD).

### 3.4.1.7 N-Point Statistics

Two-point through N-point correlation functions are a useful set of descriptors that characterize the spatial arrangement of microstructural features. Generally, these correlation functions, most common of which is the two-point correlation function, are used to analyze spatial arrangement of particles or voids in materials such as: discontinuously reinforced composites, foams, geological samples, etc. (Torquato 2002). However, correlation functions can also be utilized to describe the spatial arrangement of grains with certain microstructural parameters. For example, the spatial arrangement of grains with a given orientation in a polycrystal could be quantified using correlation functions. Two-point correlation functions can be determined by systematically placing line segments in the structure and noting where the endpoints lie. Therefore, for a microstructure with two entities, be they phases, orientations, sizes, shapes, etc., there are exactly four two-point correlation functions:  $\langle P_{11}(r) \rangle$ ,  $\langle P_{12}(r) \rangle$ ,  $\langle P_{21}(r) \rangle$ ,  $\langle P_{22}(r) \rangle$ .  $\langle P_{nm}(r) \rangle$  is the average probability that endpoint 1 and endpoint 2 of a randomly oriented line segment of length  $r$  lie in entity  $n$  and entity  $m$ , respectively (Tewari et al 2003). Note that here the term entity is being used to mean a certain property and not a

specific feature. Thus, for  $\langle P_{11}(r) \rangle$ , it is not a requirement that both endpoints lie within the same particle/feature with entity 1, just that both endpoints lie within a particle with entity 1. Two-point correlation functions can also be directionally dependent and thus, the values of each correlation function can be calculated as a function of the orientation of the line segment within the sample. The extension of two-point correlation functions to n-point correlation functions simply involves placing an n-cornered polygon, rather than a line segment, in the sample and noting the position of the endpoints. The number of functions increases with n and with the number of entities in the sample.

N-point correlation functions could be used to describe the local neighborhood around a grain in a polycrystal. A specific property of a grain, its size, for example, could be chosen as entity 1 and all other sizes could be chosen as entity 2. Then line segments of varying lengths could be drawn from the centroids of all grains with size equal to (or near that) of entity 1. The resultant two-point correlation functions would describe the spatial arrangement of grains with size equal to (or near that) of entity 1. This same process could be carried out for the Schmid factor of a grain or its orientation, which would likely offer key insight into the clustering of critical orientations.

#### **3.4.1.8 Limitations/Concerns when Using Statistical Descriptors**

The statistical descriptors presented here certainly offer a great deal of information about the microstructure, but are by no means a complete set. Other classical morphological descriptors, such as the number of faces, edges and corners of a feature have not been presented here, but are readily available in the 3D volume. Mean width was explained to be the integral of a feature's curvature and the IND analysis was shown to be the complete distribution of interface normals, but the curvatures of a grain's individual boundaries have not been correlated to the grain's size and shape or to the curvatures of neighboring boundaries. In general, the near-neighbor analyses have been limited to only contiguous neighbors and not next-nearest neighbors and beyond. These issues are not truly limitations of the descriptors themselves; rather they are an illustration of the abundant amount of information available in just one experimental volume. The limitation is actually in the ability to quantify every aspect of the structure, which has yet to be shown, is in fact necessary. It should be the goal of a concerted characterization-modeling effort to define to what extent microstructure needs to be quantified and represented for each property.

Some areas of the current analysis remain incomplete. The correlation between descriptors is one of the areas most lacking. Especially when three or more descriptors are related, it becomes difficult to quantify their dependencies on one



another. This is most frequently the result of an insufficient number of features in the interrogated volume. This can be corrected by collecting larger volumes, but limitations of experimental capabilities and availabilities may be preventative. Additionally, the statistical analyses have not yet advanced to the point of accurately informing the experimentalist of the proper number of features to collect for each type of analysis. Another area that is currently under-investigated, at least in the context of materials microstructure, is the analysis of rare events. The extreme-value statistics of the microstructure are not well understood and have not been well addressed in the quantification and comparison of structures. The standard distributions (i.e. lognormal, beta, weibull) used to describe most descriptors provide a ‘good’ fit over much of the descriptor’s range. However, when the extreme-values are closely investigated, the experimental observations often appear to deviate systematically from the fit distribution in a manner that suggests more than simply sampling error. Until the extreme-value statistics are properly quantified and accounted for in digital microstructures, simulations of properties that are believed to be controlled by rare events or neighborhoods should be treated with some sense of skepticism.

### ***3.4.2 Synthetic Structure Builders***

The synthetic builders that will be discussed here consist of two major steps. First, the features to be placed in the synthetic volume are generated. These features are generated by sampling the size, shape and morphological and crystallographic orientation distributions of the features observed by some experimental technique. Second, the features are placed in the volume with specific focus on the local neighborhoods created by neighboring features. The sampling procedure for generating representative features as well as the constraints used to place the features in the volume will be described here. Figure 10 shows some example synthetic volumes generated by the different techniques discussed in this section.

#### **3.4.2.1 Representative Feature Generation**

A representative feature generation process is responsible for the creation of a collection of idealized ellipsoidal (or alternative representation) features having distributions of size, shape and morphological and crystallographic orientation equivalent to those observed in the experimental volume. In this representation, each grain is modeled as an ellipsoid as defined in the previous section on feature shape. The size corresponds to the volume of each ellipsoid, the shape corresponds to the aspect ratios of the principal axes ( $b/a$ ,  $c/a$  and  $c/b$ ) and the morphological orientation corresponds to the orientation of the major principal axis ( $a : a \geq b \geq c$ ) relative to the global coordinates. The first step in the process is

to sample the experimental feature volume distribution, which is represented by the cumulative probability distribution function (CPDF) fit to the experimental data. Many investigations have shown the feature volume distribution to be best represented by a lognormal distribution (Zhang et al 2004, Groeber et al 2008), whose CPDF is given by:

$$P(V) = \begin{cases} \frac{1}{2} \left( 1 - \operatorname{erf} \left( \frac{V_g^{AVG} - V}{V_g^{STD} \sqrt{2}} \right) \right) & \rightarrow V < V_g^{AVG} \\ \frac{1}{2} \left( 1 + \operatorname{erf} \left( \frac{V - V_g^{AVG}}{V_g^{STD} \sqrt{2}} \right) \right) & \rightarrow V > V_g^{AVG} \end{cases} \quad (3.12)$$

where,  $V$  is the feature volume,  $P(V)$  is its cumulative probability, which has 0 and 1 as its limits. The average feature volume ( $V_g^{AVG}$ ) and the standard deviation ( $V_g^{STD}$ ) are parameters that determine the precise shape of the distribution function. During volume assignment, a number within the limits of  $P(V)$  is randomly generated and the corresponding volume, given by equation 1, is assigned. This assignment process is continued until the total volume of all features generated equals a threshold defined as 110% of the volume of the synthetic microstructural model. The additional volume is needed because some features may lie partially outside the domain of the microstructural model or overlap other features. This issue will be discussed further in the next subsection.

Subsequent to the volume assignment, feature shapes are assigned in conformity with CPDFs of the ellipsoid aspect ratios ( $b/a$ ,  $c/a$  and  $c/b$ ) that have been established a priori from the experimental data. The corresponding CPDFs can be represented in terms of a beta distribution, with the form:

$$P(b/a) = \frac{\int_0^{b/a} t^{p-1} (1-t)^{q-1} dt}{B(p, q)}, \quad 0 \leq b/a \leq 1 \quad (3.13)$$

In equation 3.13,  $B(p, q) = \int_0^1 t^{p-1} (1-t)^{q-1} dt$  is the beta function,  $p$  and  $q$  are

the shape parameters and  $P(b/a)$  is the cumulative probability. The statistical analysis establishes the correlation between the shape and the size of each grain, represented by the aspect ratios and volume of each ellipsoid. To establish this correlation for the synthetic ellipsoidal features, each volume is converted to an equivalent sphere diameter ( $ESD$ ) using the relation:

$$ESD = 2 \cdot \left( \frac{3}{4\pi} V \right)^{\frac{1}{3}} \quad (3.14)$$

The correlation is determined by assigning aspect ratios to different volumetric bins that are represented by ranges of  $ESD$  values. The two aspect ratios that define an ellipsoid ( $b/a$  and  $c/a$ ) each have a CPDF in each volume bin. The sampling of the  $b/a$  and  $c/a$  CPDFs is identical to that of the feature volume CPDF. This process ensures appropriate correlation between the shape and size distributions.

In addition to a correlation with volume, the aspect ratios  $b/a$  and  $c/a$  should also be mutually correlated. However, often there is an insufficient number of features in the experimental volume to determine this correlation table between the grain volume  $V$ , and both of the aspect ratios  $b/a$  and  $c/a$ . To overcome this shortcoming, individual correlation functions are generated between  $V$  and each of the aspect ratios separately. In this process, values of  $b/a$  and  $c/a$  are evaluated corresponding to randomly chosen  $P(\frac{b}{a})$  and  $P(\frac{c}{a})$  values from the  $P(\frac{b}{a}) - (\frac{b}{a})$

and  $P(\frac{c}{a}) - (\frac{c}{a})$  plots, respectively. The consequent aspect ratio  $\frac{c}{b} = \frac{c}{a} \div \frac{b}{a}$  is evaluated and its probability density

$$p(c/b) = \frac{(c/b)^{p-1} \cdot (1-c/b)^{q-1}}{B(p,q)}, \quad 0 \leq c/b \leq 1 \text{ is ascertained from the}$$

experimentally observed distribution. The two individually generated aspect ratios are accepted with the same probability density of  $p(c/b)$ .

The third variable, the morphological orientation of each ellipsoidal feature, is defined by a set of rotations  $(\theta, \lambda, \psi)$  needed to transform the global coordinates  $(X, Y, Z)$  onto the principal axes of the ellipsoid  $(A, B, C)$ . The probability density

function,  $f(g)\Delta g = \frac{\Delta N_g}{N}$  is the probability of observing an orientation  $G$  in

the interval  $g \leq G \leq g + \Delta g$ , where  $\Delta N_g$  is the number of orientations between  $g$  and  $g + \Delta g$  and  $N$  is the total number of experimentally observed ellipsoidal features. If  $N^{(i)}$  is the number of observations in the  $i$ th orientation space element ranging from  $(\theta, \lambda, \psi)$  and  $(\theta + \Delta\theta, \lambda + \Delta\lambda, \psi + \Delta\psi)$ , then the density of orientations can be expressed as  $\frac{N^{(i)}}{N}$ .

To evaluate this density, the entire orientation space is defined as a finite cube with edge length  $\pi$  ( $180^\circ$ ) with the ori-

gin at one of its vertices. For the purpose of creating ranges in the orientation data, the orientation space is discretized into cubic bins of dimension  $\pi/36$  or  $5^\circ$ . The morphological orientation density in each bin is calculated by dividing the number of orientations in the bin by the total number of orientations in the experimental data and normalizing by the size of the bin. Ellipsoidal orientations are created and assigned based on this probability density function.

In summary, the output of this process is a set of representative ellipsoidal features having statistically equivalent volume, aspect ratio and morphological orientations as the experimental reference data. However, this process does not arrange the features in their appropriate spatial locations, which is the function of the next process. A final step in this procedure can be included either before or after the feature placement routine. This step is the assignment of crystallographic orientations to the generated features. The process of assigning crystallographic orientations is exactly identical to that of the morphological orientation assignment process previously described. Here the only difference is that the rotations assigned are those to transform the global coordinate axes to the coordinate system of the crystal, rather than the principal axes of the grain.

#### **3.4.2.2 Feature Placement**

After generating a set of ellipsoids that is representative of the 3D features, the focus must be shifted to the placement of the ellipsoids in the volume. There are multiple issues to consider when packing the ellipsoids. The density of the objects represented by the ellipsoids is one of the largest factors in developing the packing algorithm. For example, ellipsoids representing particles of a low volume fraction phase will certainly be placed differently than ellipsoids representing grains in a fully dense polycrystalline material. In the fully dense grain example, care must be taken to pack the volume as densely as possible, but minimize overlap between ellipsoids in order to retain each ellipsoid's prescribed shape. In both cases, the local neighborhood of the ellipsoid (i.e. neighboring ellipsoids) must also be addressed during placement. The low volume fraction particles should be spaced equivalently to the experimental/reference data and the densely packed grains should neighbor grains of similar sizes and shapes as seen in the experimental/reference data.

Two inherently different, but viable options for ellipsoid packing will be discussed here. The first approach involves overpopulating the volume with a large number of ellipsoids. This approach is presented in greater detail elsewhere (Saylor 2004, Brahme 2006). A large set of representative ellipsoids are placed into the model volume. The ellipsoids should have a total volume much larger than the volume to be filled and are allowed to overlap and extend outside of the volume. A simulated annealing procedure can then be employed to determine an "optimal"

set of ellipsoids. An optimal set of ellipsoids would maximize space-filling, while minimizing overlap of ellipsoids. Saylor (2004) and Brahme (2006) outline the development of a penalty function that promotes optimal space filling. It is easy to imagine the adjustment of this function to address the less dense packing of the distant particle case. At present, only the space-filling nature of the ellipsoids is addressed in this technique and not the local neighborhood of an ellipsoid. However, it is conceivable that penalty functions could be developed to encourage desired clustering or spacing of ellipsoids of given sizes or shapes. Once an active set of ellipsoids are selected by this method, a voxelized structure is generated using Cellular Automata (CA) where the centroid for each ellipsoid is a seed point in the simulation and voxels are added starting at this seed point until the entire structure is filled. The growth is constrained initially such that only those voxel locations that are located inside the ellipsoids are added. When each ellipsoid is completely filled then the constraint is dropped and the remaining free volume is consumed.

A second approach to the ellipsoid packing problem is to sequentially place the ellipsoids while using statistical descriptors from the experimental/reference data as constraints. One such implementation of this approach is presented by Groeber et al (2008). Here, the set of representative ellipsoids should have a total volume much nearer to the model volume than the first approach. The ellipsoids are allowed to extend outside the volume, similar to the first approach, and thus the total volume should be some small amount (i.e. ~10%) above the model volume. Each ellipsoid is randomly placed in a sequential fashion and checked against a number of constraints to determine if its current position is acceptable. Constraints can include, but are not limited to: overlap limits, number of neighboring ellipsoids and size distributions of neighboring ellipsoids. This approach generally yields optimal space-filling through the overlap limits and produces realistic neighborhoods by constraining placement to locations that improve the surroundings of previously placed grains. Though this technique presents some advantages over the previous, there are complications that arise as well. In any sequential process there should be concerns of a failure to locate a suitable position, especially near the end of the process. Generally, the process is more efficient and successful when the largest grains are placed first, when there is sufficient room left for their placement. Additionally, the number of constraints greatly affects the feasibility of locating a suitable position and thus should be optimized.

### ***3.4.3 Measures of Goodness***

The ‘goodness’ of the synthetic structure can be defined relative to two objectives, which may or may not be completely related. First, the statistical descriptors of the synthetic structure can be compared to those of the experimental struc-

ture. The similarity of these descriptors is certainly one measure of ‘goodness’ and will be a focus of the following subsections. Second, the simulation results of the two structures can be compared. This definition of ‘goodness’ is arguably a more practical one, in that the response of the material is often the overriding goal. However, depending on the property of interest, the two structures may be ‘equivalent’ with respect to the statistics chosen, but still yield different simulation results. This is likely to be the case when the experimental structure is smaller than a representative volume element (RVE) for the specific property or the statistical descriptors chosen are not directly linked to the response property. This section will not deal with the second definition; due mainly to a lack of simulation results, but it should be considered carefully in future structure-property relation investigations.

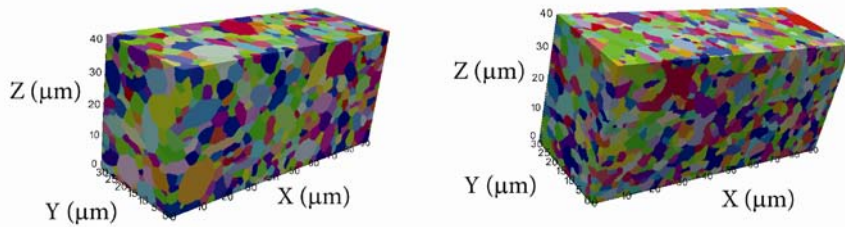


Figure 10: Example synthetic structures produced by (left) the sequential grain placement algorithm using ellipsoidal grains and (right) the sequential grain placement algorithm using superellipsoidal grains. Note that the grains generally appear less “idealized” in the right image where the superellipsoid representation described section 3.4.1.2 was used.

### 3.4.3.1 Size(s)

Measuring the “size” of a grain may appear to be a simple matter at first sight. Even in 2D sections, however, computing the circle-equivalent diameter yields a (slightly) different result than the average linear intercept (Underwood 1970). In 3D, one must be concerned with all three dimensions, of which measuring the volume and surface area of a grain is intuitively obvious. Less obvious is how best to measure the linear dimension of a grain, since there are so many possibilities (linear intercept, sphere-equivalent radius, etc.). The recent publication by MacPherson and Srolovitz (2007) on the theory of grain growth has, however, pointed out to the materials science community that “mean width” is not only a useful measure of integral curvature of objects such as grains, but that it also is unique in its property of additivity. Hadwiger (1957) showed that there is only one measure in each dimension that has the property of additivity, which means that the volume/area/mean width of the union of two overlapping objects is the sum of the separate quantities, minus the volume/area/mean width of the overlapping region.

This suggests that the distributions of the three basic quantities (volume, area and mean width) should be part of the validation of a digital microstructure. Moreover, ratios between pairs of these quantities, as shown in Figure 11, also provide basic information on the shape of objects. Fitting to distributions of such ratios may also be part of the development of feature geometry in 3D models.

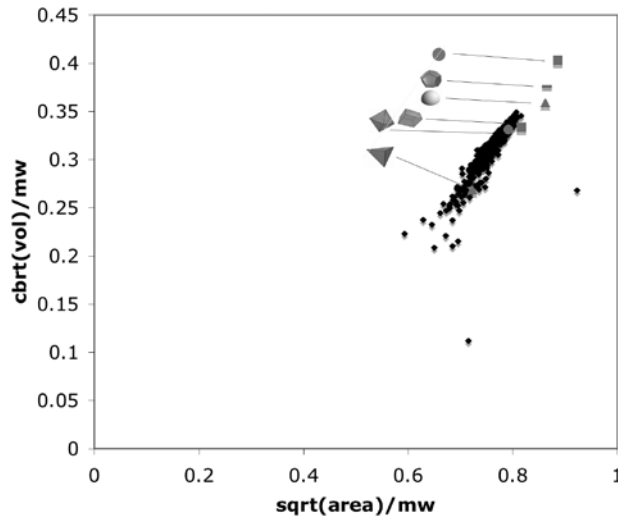


Figure 11: Blasche diagram combining the properties that exhibit additivity in the three dimensions. The x-axis is the square root of surface area normalized by mean width and the y-axis is the volume normalized by mean width. The positions where some standard geometrical shapes reside on the plot are noted.

### 3.4.3.2 Shape(s)

A typical approach to quantifying the shape of grains is to fit an ellipsoid and report the aspect ratios (Groeber et al 2008, Saylor et al 2004). This approach is useful in describing the distribution of the amount of elongation of the grains. However, aspect ratios are ambiguous in reference to many aspects of shape. For example, it is possible for an ellipsoid and a rectangular prism to have the same set of aspect ratios. The local curvatures of grain boundaries are often disregarded when a ‘simple’ geometric feature is fit to represent a grain. It is this issue that makes shape one of the more complicated parameters to describe.

MacSleyne et al (2008) have presented a method for distinguishing shapes by utilizing all three of the second order moment invariants. The moment invariant technique creates a three-dimensional moment invariant space to represent a

grain's shape rather than the limited two-dimensional space defined by a pair of aspect ratios. In the moment invariant space, shapes with similar aspect ratios lie on the same arc, but are separated along the third dimension,  $\Omega_3$ . Additionally, combinations of the calculated moments can yield interesting insights into the types of shapes present in the structure. An example of a moment invariant analysis is shown in Figure 12. The analysis provides the distribution of aspect ratios, which appears roughly equivalent for the two structures. However, when the value of  $\Omega_3$  is compared, there is a noticeable shift in the distribution between the two structures. Finally, the largest difference between the two structures can be seen in the comparison of the distribution of  $V/V_{\text{conv}}$ .  $V_{\text{conv}}$  is the volume of the convex hull of the grain and  $V$  is the volume of the grain itself. The ratio of these two volumes is bounded by 0 and 1 and compares the relative concavity of the grain. It should be clear that the aspect ratio comparison alone does not accurately highlight many of the differences between the shapes in the two structures.

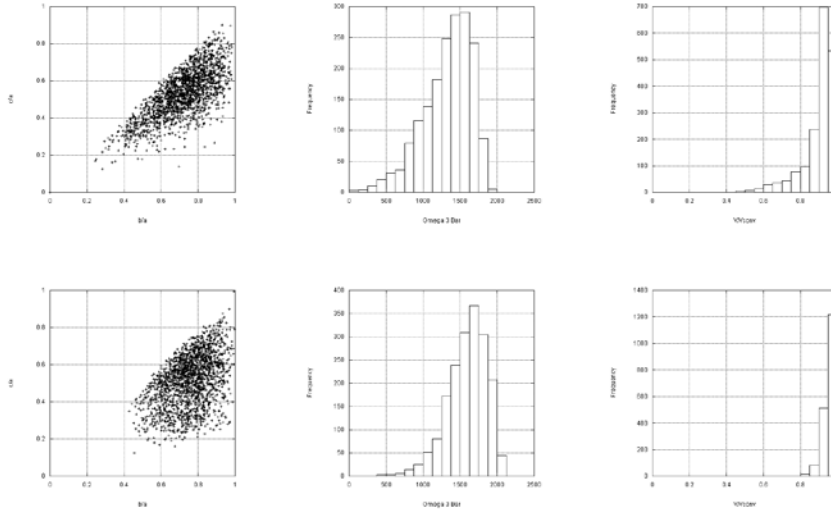


Figure 12: Example of results from a moment invariant analysis. The upper set of plots is from an experimentally collected volume (Groeber 2008). The lower set of plots is from a synthetic microstructure generated with the goal of matching the experimental volume's statistics, using methods presented by Groeber (2008). The analysis highlights the need (and ability) to look past lower order descriptors like aspect ratios.

### 3.4.3.3 Neighborhood(s)

The local neighborhood of a grain can be a complicated aggregate of features that can be described by a number of different parameters. For example, the mor-



phological descriptors of the neighboring features could be reported or their crystallographic relationship to the reference grain could be of more interest. Additionally, the approach to describing the local neighborhood of grain is likely to vary with the type of microstructure and data being investigated. A grain structure which has been segmented is likely to have a known connectivity of grains and contiguous neighbors can be characterized. In the case of low volume fraction second-phase particles, the nearest neighbors may not be known and a two-point statistics approach (Gokhale , Kalidindi) may be better suited.

For describing the morphology and connectivity of a grain's neighborhood, there are multiple distributions that can be created. First, the distribution of number of neighbors can be generated for all grains, as well as correlated to grain size by grouping grains of similar size. In addition to number of neighbors, the size distribution of the neighboring grains can also be considered. The size distribution of neighbors, when correlated to the size of the reference grain, offers insights into the tendency of grains of certain sizes to cluster together (i.e. Aboav-Wieve). The shapes of neighboring grains can be correlated to the reference grain's shape to quantify the clustering of similar shaped grains, which may evolve during recrystallization or deformation.

The crystallographic description of individual boundaries will be discussed in the next section, but there are other parameters that describe the crystallography of local grain aggregates to varying degrees. The misorientation distribution function (MoDF) can be calculated for the entire structure, which gives some insight into the local textures present in the material. However, the MoDF does not provide any knowledge of the spatial distribution of the misorientations in the MoDF. The known connectivity of the grains allows for the spatial description of the misorientations. For example, one could calculate the fraction of a grain's neighbors that have a critical misorientation value, be it high, low or special. This approach could then be expanded to include secondary neighbors (i.e. neighbors of neighbors) and would ultimately offer a more local estimate of the clustering of grains with similar orientation. Two-point statistics can also be employed to describe distributions of orientations as well.

#### **3.4.3.4 Boundary Character(s)**

In order to generate a complete 3D microstructure, one must add grain (crystal lattice) orientations to the description. The current state-of-the-art is that the grain geometry is created first and then a set of orientations is optimized with respect to texture and grain boundary misorientation (Saylor et al 2004, Groeber et al 2008). The procedure relies on simulated annealing and is computationally straightforward on modern personal computers. This procedure has at least two significant limitations, however. The first is that it assumes that size and shape are uncorre-

lated with orientation. However, this is not always the case; Bozzolo et al. (2005) have demonstrated that in titanium that has been deformed and then recrystallized there are texture components that are more dominant in the small grains and vice versa. The second limitation is that it ignores the fact that grain boundary properties depend on the interface normal as well as the lattice misorientation across them. The full description of grain boundary character requires, in fact, five macroscopic parameters. Fitting orientations to include both texture and misorientation and interface normal distributions needs to be developed. Implementing such an algorithm in voxel-based representations requires some method to compute the local interface normal. Alternatively, interface normals are straightforward to compute in a surface or volumetric mesh representation of a microstructure, which has been discussed previously.

### **3.5 Inference of 3D Structure**

It is often the case that the true 3D structure of a material is not available to include directly in a computational model. This can be attributed to the cost, availability and complexity of experimental tools. As a result, it is still a reality for many to infer 3D structure from 2D observations. As previously mentioned, if 3D statistical descriptors can be inferred from 2D observations, the synthetic structure builders discussed in the previous section can be used to generate 3D structures for simulation. The following section will discuss some potential methods for inferring 3D statistics from 2D observations.

#### ***3.5.1 Link Between 2D and 3D Structure***

The statistical reconstruction method described here is based on limited cross-sectional information from a given material; it is essential, however, that cross-sections are made on more than one sectioning plane, and preferably on three orthogonal planes. Statistical methods for reconstructing microstructures have been developed in a number of fields, especially for modeling geological materials (Fernandes 1996, Oren 2002, 2003, Sundararaghavan 2005, Talukdar 2002). Saylor et al. proposed a method of constructing 3D models of polycrystalline materials based on the microstructural features observed in three orthogonal sections (Saylor 2004). In this report the microstructural features of interest include size and shape of grains, misorientation distribution, orientation distribution, and the relative placement of grains with respect to size. The procedure outlined by Saylor, along with adaptations for elongated grain shape noted by Brahme (2006) is the basis for one of the procedures described here. Groeber (2007) also offered a methodology for inferring 3D structure from 2D measurements. In Groeber's

study, the 2D sections were obtained by sectioning synthetically generated 3D structures, which provide a known set of 3D statistics to compare with the inferred statistics.

There is a substantial literature on the general stereological problem of reconstructing 3D microstructures based on limited section information. When treating microstructures as collections of general particles whose size, shape and orientation are to be reconstructed (without regard to their packing), the problem is known to lack a solution (Cruz-Orive 1976). However, for particles that are monodisperse (in size and shape), this problem is well known and has semi-analytical solutions for which the names Cahn and Saltykov are well known in the materials literature (Cahn 1956, Saltykov 1958). For a historical overview, see Underwood (1970). In contrast to these more general cases, polycrystalline grain structures have an added constraint since grains are not independent particles (i.e. low volume fraction) because they fill space. This constraint enhances the ability to accurately reconstruct a 3D distribution from 2D observations (Przystupa 1997). This section will attempt to address the previously less investigated problem of space-filling particles (i.e. grains).

### ***3.5.2 Probable Set Generation***

#### **3.5.2.1 Monte-Carlo Histogram Fitting**

In this section an example of generating a set of 3D (ellipsoidal) grains using statistical distributions calculated on three 2D, orthogonal, EBSD-based micrographs is given. The grain size distributions for the three orthogonal planes of a rolled aerospace aluminum alloy are shown in Figure 13. Matching the statistics in the generated 3D structure to the measured 2D statistics is accomplished through a multi-step process that includes: (1) generating representative ellipsoids (in terms of size and shape distributions), (2) placing those ellipsoids into a volume, (3) allowing that volume to be filled with voxels that are grouped as grains, and (4) modifying the grain structure by use of a (isotropic) Monte Carlo grain growth (Rollett et al 2004). The first step in this process is the focus of this section, while the latter steps were previously discussed in the section on feature placement during synthetic structure generation.

The transition from 2D to 3D is accomplished by assuming the grain shape is that of an ellipsoid and considering that the observations on 2D sections are only a portion of the true size and shape of the actual grain. The probability distribution functions (PDFs) of the ellipse dimensions obtained from the sliced ellipsoids are

given as  $f'(a), f'(b)$ , where  $a$  and  $b$  are the semi-axes of an ellipse, and the prime accent indicates that it is from a section. In this case the ellipse dimensions are assumed to be independent, and that  $a > b$ . References to the cumulative distribution function, CDF, utilize the same notation but with a capital “F”. The input data is used directly to create a CDF (i.e.  $F(TD)$ ) of grain size where the range of the CDF is 0 to 1 and the domain is scaled in micrometers. The distribution for each direction is sampled and multiplied by a stereological constant to account for the fact that the CDF is generated from a 2D section. In this approach the total number of ellipsoids generated is specified as input to the program and it proceeds to optimize the list such that they are a good match to the input data. The optimization is accomplished iteratively and the first step is to create an initial list of ellipsoids and then slice each of them many times and extract the 2D CDFs of grain size on each section. The RMS error between list and the input data is computed. The initial list is then modified by generating a new ellipsoid in the same manner as before and then randomly choosing an ellipsoid to replace from the list. The ellipsoid is replaced only if the new ellipsoid lowers the error of the system. The program completes when it has performed a number of user specified iterations. The result of this method can be observed directly by comparing the PDFs and CDFs of the data and the simulated ellipsoids directly as can also be seen in Figure 13. The distributions in both the ND and TD directions are well matched to the input data. The discrepancy on the RD direction in this case is due to improper sampling of the grains in the RD direction (i.e. the majority of grains intersected the scan boundary).

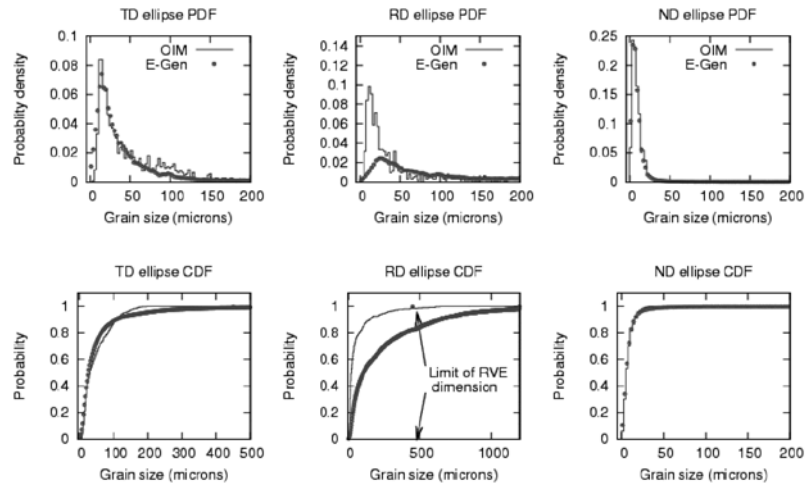


Figure 13: The resulting (top) PDFs and (bottom) CDFs for the OIM input data and ellipsoids generated to represent the data for the ND, RD, and TD directions.

### 3.5.2.2 Domain Constraint

The elemental assumption of this method is that the entire (and infinite) set of all possible ellipsoids can be bounded by observations of ellipses on experimentally collected, orthogonal 2D sections to leave a “most probable” set of ellipsoids. Factors such as the distributions of size, shape and orientation of the ellipses on the 2D sections are used to assign probabilities to groups of ellipsoids. This type of an approach is fundamentally different than the analytical developments made by Cruz-Orive (1976) and DeHoff (1962) in that an exact solution is not the goal, rather a probable set is desired. An initial description of this technique is introduced by Groeber (2007).

In order to assign probabilities to groups of ellipsoids, the infinite domain of ellipsoids must be initially truncated and discretized. A five dimensional space is created to define the ellipsoids. Three dimensions correspond to the orientation of the principal axes of the ellipsoid and are inherently bounded by the finite dimensions of Euler space, which describe the orientation of the ellipsoid (i.e. its principal axes). The other two dimensions correspond to the two aspect ratios of the ellipsoid. The aspect ratio dimensions are not inherently bounded, but can be truncated by using the 2D observations to make assumptions about reasonable upper and lower bounds. By definition, the upper limit of the two aspect ratio dimensions is 1 (i.e. a sphere) and the lower limit can be set to be the smallest aspect ratio observed in the 2D sections. In practicality, the accuracy of the estimated lower limit will be directly related to the number of observations and thus, it may be prudent to reduce the minimum observed value by an additional 25-50%. The volume of the ellipsoids is treated only as a distribution within each discrete bin in the 5D space, not as its own dimension. This is because volume only scales the dimensions of an ellipsoid and any resultant elliptic section through it, which has no effect on the following process.

Development of a probable set of ellipsoids is undertaken as an iterative process because of the inability to decouple the influences of ellipsoid shape (aspect ratios) and orientation on the resultant distribution of ellipses. The iterative process initiates by calculating a probable orientation distribution for the ellipsoids with an assumed uniform shape distribution. Then the shape distribution is updated using the calculated orientation distribution. Iteratively, each distribution is updated using the most recently calculated instance of the other distribution until a level of convergence is reached. Some details of the calculations are offered here as well as the process of extrapolation of the individual ellipses.

Calculation of a probable orientation distribution requires sectioning a large number of ellipsoids within each discrete orientation bin and observing their resultant elliptic sections. Each ellipsoid is assigned a set of aspect ratios in accordance with the shape distribution, which is initially uniform. A two-dimensional

histogram of resultant ellipse orientation and resultant ellipse aspect ratio is created for all ellipsoids in each of the orientation bins. An example histogram, shown as contour plots, is shown in Figure 14. The histograms for each orientation bin are then compared to the same histogram made from the actual observations on the experimental 2D sections. The simulated histograms are fit to the experimental histogram by a least squares method to determine the probability of each orientation bin.

Upon calculating the orientation probability distribution, the shape distribution can be updated by sectioning a large number of ellipsoids within each discrete shape bin, represented by a set of aspect ratios. Each ellipsoid is assigned an orientation in accordance with the previously calculated orientation distribution. A two-dimensional histogram of resultant ellipse aspect ratio and resultant ellipse normalized size is constructed for all ellipsoids in each of the shape bins. The normalized size is the area of the resultant ellipse divided by the average resultant ellipse area. An example histogram is shown in Figure 14. The histograms for each shape bin are then compared to the same histogram made from the actual observations on the experimental 2D sections. The simulated histograms are fit to the experimental histogram by a least squares method to determine the probability of each shape bin.

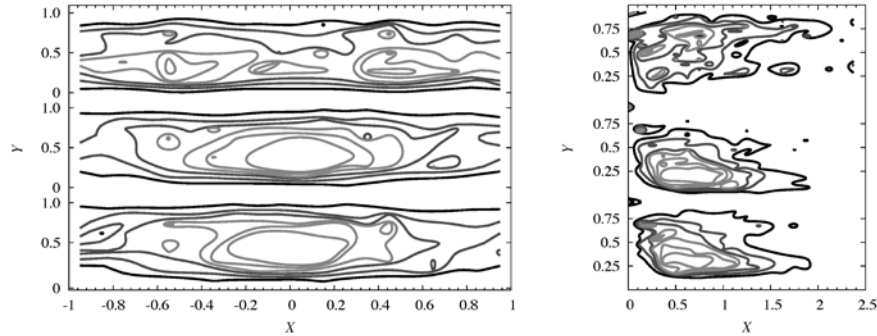


Figure 14: Plot of (left) density of ellipse principal axis orientation vs aspect ratio and (right) density of ellipse normalized size vs aspect ratio. The top third of each plot shows ellipses on the plane normal to the z-direction, the middle third shows ellipses on the plane normal to the y-direction, and the bottom third shows ellipses on the plane normal to the x-direction. In the left plot, the x-axis refers to the x-component of a unit vector oriented along the major axis of the ellipse and the y-axis is the aspect ratio (b/a) of the ellipse. In the right plot, the x-axis is the ellipse area divided by the average ellipse area and the y-axis is the aspect ratio (b/a) of the ellipse.

While sectioning the ellipsoids to determine a probable orientation and shape distribution, the distribution of fractional section size is constructed for each shape

bin. The fractional section size is defined as the resultant ellipse area divided by the maximum possible resultant ellipse area for a given ellipsoid (i.e. when the ellipsoid is sectioned through the equatorial plane perpendicular to the minor axis). The fractional section size distribution is used to extrapolate the individual experimental ellipses. The shape of each experimental ellipse's parent ellipsoid is predicted by the probability of an ellipsoid of a given shape producing the experimental ellipse (i.e. its normalized size and aspect ratio). Once the parent ellipsoid's shape is assumed, the distribution of fractional section size for that shape can be used to convert the experimental section's area to the maximum possible section area for the parent ellipsoid. With an assumed shape and maximum possible section size, everything necessary to fully define the parent ellipsoid is available. This process is carried out for each experimental ellipse, resulting in a set of 'probable' ellipsoids whose statistics can be used to generate synthetic 3D volumes. Figure 15 shows the results of the observation-based domain constraint process for a sample microstructure.

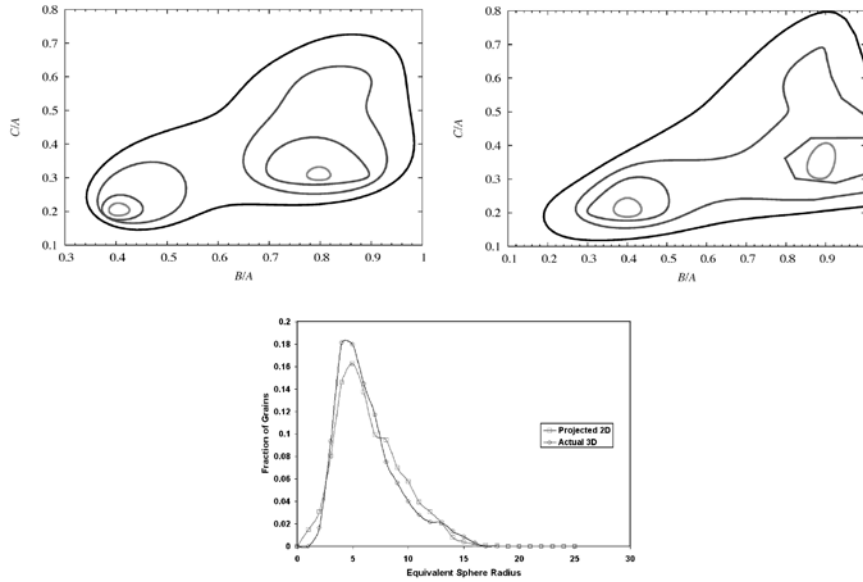


Figure 15: Results of the Observation-Based Domain Constraint method. The upper right image is the true 3D shape distribution (ellipsoid aspect ratios). The upper left image is the 'probable' shape distribution calculated by the method. The lower image is a comparison of the true 3D grain size distribution (equivalent sphere radius) and the calculated 'probable' size distribution.

### ***3.5.3 Limitations and Possibilities***

Currently, there are a number of limitations that remain when inferring the true 3D microstructure of materials. First, the shape of the features being inferred has been limited to simple geometric shapes that can be easily described numerically, generally ellipsoids. This limitation need not be persistent, provided numerical descriptions of more complex shapes are developed. The moment invariant analysis mentioned previously may provide a key tool in developing this area.

Additionally, the linkage between neighborhoods of grains in 3D and grains in 2D is not immediately clear to this author. The number of neighbors, as well as their size, shape, etc, is likely to be a function of the packing of the grains, which may not be known from even several 2D sections. In principle, it would be possible to section many different, yet known, microstructures and attempt to develop a “look-up” table that correlates parameters such as: number of 2D neighbors to number of 3D neighbors.

## **3.6 Comments on Complex Microstructures**

The microstructures investigated in the works presented in this chapter are relatively idealized. The nickel-base superalloy used in the work of Groeber et al was chosen for its small feature size, propensity to yield high quality data and microstructural homogeneity. The aluminum alloy used in the work by Saylor et al and the steel used in the work by Rowenhorst et al both are single phase materials with standard boundary structures and limited heterogeneities. These properties enabled the investigation of microstructure with comparatively little difficulty. All three microstructures certainly have inherent difficulties as well. The nickel-base superalloy contains a second phase that is difficult to distinguish from the matrix as well as twin grains that are often too small to sample properly with the tools used. The rolled aluminum alloy has a grain size too large for the desired experimental techniques (i.e. EBSD). The steel required the precipitation of a second phase to identify boundaries easily, which was met with some difficulty. However, the complications encountered do not approach the level of some heavily engineered, more topologically complex microstructures, such as beta-processed titanium with a basketweave structure. Techniques are being expanded to treat such microstructures, but are currently in the developmental stages.

It should not be a surprise that for the advancement of digital representation of grain-level microstructure to include more complex microstructures, there must be a coupled advancement in the ability to collect and quantify these microstructures. Additionally, clever techniques to homogenize or adaptively incorporate multiple



microstructural scales will be an imperative to simulate microstructures that have critical features that exist of varying length scales. The utility of a microstructure representation can be limited greatly if the computational modeling community has no feasible method to simulate the structure. Again, this calls for a representation-modeling effort that defines the degree to which microstructure needs to be incorporated, both in the context of its effects on the property and on its ability to be simulated. For the example of beta-processed titanium, Ghosh et al. (2008) have developed a homogenized grain representation that homogenizes the lamellar/lath structure of the titanium, which would be impossible to incorporate at the scale needed to include hundreds of prior beta grains. Thus, for properties that this homogenization is proper, the experimental techniques and representation tools can be tailored to identify and represent only the prior beta grains (and alpha colonies/variants) and omit the underlying lath-rib structure in an effort to increase simulation efficiency.

Lastly, the synthetic structure generation process should likely attempt to parallel the natural process that produced the microstructure of interest. That is, the application of an increasing number of generic constraints on the placement of features in the synthetic volume is likely to inhibit the generation process. However, if the generation process follows the natural process, then many constraints may become obsolete and unnecessary. Two examples of this idea are the inclusion of twin grains in a polycrystal and the generation of a colony (or basket-weave) structure in a titanium alloy. In the case of twin grains, it is difficult (if not impossible) to treat the twin and its parent grain as independent features and ensure that they will be placed in proper relation in the synthetic structure. Rather, it is potentially a better strategy to remove the twin grains, by merging them with their parent grains, and characterize the simplified structure. Then, a synthetic structure without twins can be generated to match the simplified structure. If the statistical description of the twin structure (i.e. fraction of grains with twins, twin plate thickness, number of twins per grain, etc.) is measured during the merging, then twins could be inserted into the simplified synthetic structure, which would simulate the natural process of twin nucleation in a parent grain. In the case of the colony structure of a titanium alloy, if the colonies themselves are treated as the features to be placed, it is a complicated process to place colonies into neighborhoods that have the proper orientation relationships (in accordance with the Burgers' relationship) and the correct topological structure (imposed by the prior beta grain boundaries). One option to circumvent this complication is to generate a synthetic structure that consists only of prior beta grains, with the statistics to match the experimental beta grain structure. The prior beta grains can be identified by grouping the colonies that came from the same beta grain, which is known through the Burgers' relationship. Then, the synthetic beta grains can be divided into colonies, where the orientations are already constrained by the beta orientation and the topology is already constrained by the beta grain boundaries. Similar to the twin example, the statistics of the 'secondary' features (i.e. the twins or co-

lonies) can be measured during grouping to locate the primary features (i.e. the parent grains or prior beta grains). Dividing the beta grains into colonies simulates the natural precipitation of the alpha phase in the prior beta grains. Linking the synthetic generation process to the natural process may simplify the representation of complex structures and it is also likely to enhance the physical significance of the generated structure.

### **3.7 Conclusions**

This chapter has attempted to discuss the key areas necessary for the development of digital representations of materials microstructure at the grain level. Much of the detail in the various areas is presented elsewhere and as been noted wherever possible. It was the goal of the author to highlight the current ‘state-of-the-art’ techniques and discuss their strengths and weaknesses. This field is still in a state of relative infancy and requires the cooperation of a number of other fields to properly evolve. The experimental community has elevated the ability and precision with which it can investigate microstructure in the last decade. It is important for communication with this community to tailor experiments to the needs of given representation requirements. After the generation of a microstructure representation, mesh generation remains a barrier to the simulation of models (without artifacts). The general meshing community has not been introduced to the needs of the materials modeling problem. Quantification of mesh error relative to the digital representation is one key metric, as well as the quality of elements required for a given simulation. Lastly and arguably the most critical, the development of a connection between simulation results and statistical descriptors is imperative. Such an association is a necessary part of the pathway to the determination of a representative volume element (RVE) for all materials properties. The improvement of constitutive relations requires knowledge of what descriptors influence properties and proper quantification of descriptors is key in defining their influence on properties. Digital representation of materials microstructure is an integral part in the determination of microstructure-property relationships, but cannot be treated as an independent step in the process. The full effect of developments presented here and those to come will only be realized when these collaborations have been cultivated.

### **Acknowledgments**

The author would like to acknowledge his collaborators, all of whom contributed through detailed discussions and in many cases developed some of the tools and techniques presented in this chapter. All of the sections in this chapter were

heavily influenced by them and in some instances their own words and terminology were used. The works of Profs. Tony Rollett and Somnath Ghosh; as well as Drs. David Rowenhorst, Dennis Dimiduk, Mike Uchic, Sukbin Lee, and Mrs. Yash Bhandari and Steve Sintay and many others have greatly advanced this field and inspired this author.

## References

- Bhandari Y, Sarkar S, Groeber M, Uchic M, Dimiduk D, Ghosh S et al (2007) *Comp Mater Sci* 41:222–35
- Brahme A, Alvi MH, Saylor D, Fridy J, Rollett AD (2006) *Scripta Materialia* 55:75-80
- Bozzolo N, Dewobroto N, Grosdidier T, Wagner F. (2005) *Mater Sci Eng A - Structural Materials Properties Microstructure And Processing* 2005;397:346
- Bullard, J. W., E. J. Garboczi, Carter, W. C., Fuller, E. R. (1995) *Comp Materials Sci* 4:103-116
- Budai JD, Yang W, Larson BC, Tischler JZ, Liu W, Weiland H, Ice GE et al (2004) *Mater Sci Forum* 467-470:1373-1378
- Budai JD, Liu W, Tischler JZ, Pan ZW, Norton DP, Larson BC, Yang W, Ice GE et al (2008) *Thin Solid Films* 576:8013-8021
- Cahn JW, Fullman RL (1956) *Trans Metall Soc of AIME* 206:610-612
- Cruz-Orive LM (1976) *J Microscopy* 107:1-18
- Cruz-Orive LM, (1976) *J Microscopy* 107: 235-253
- Dehoff RT (1962) *Trans Metall Soc AIME* 224:474-486
- Dillard SE, Bingert JF, Thoma D, Hamann B (2007) *IEEE Trans Visual Comp Graphics*
- Feltham P (1957) *Acta Metall* 5:97-105
- Fernandes CP *et al.* (1996) *Physical Review E* 54:1734-1741.
- García RE *et al.* (2004) In: Raabe D (Ed) *Continuum Scale Simulation of Engineering Materials*, Wiley-VCH, Weinheim, Germany; <http://www.ctcms.nist.gov/oof/index.html>
- S. Ghosh, Y. Bhandari and M. Groeber, “CAD based Reconstruction of three dimensional polycrystalline microstructures from FIB generated serial sections”, *Journal of Computer Aided Design*, Vol. 40/3 pp 293-310, 2008.
- Groeber MA, Haley B, Uchic MD, Ghosh S. et al (2004) In: Ghosh S, Castro J, Lee JK, (Eds) *Proceedings of NUMIFORM 2004*, AIP Publishers Melville, NY
- Groeber MA, Haley BK, Uchic MD, Dimiduk DM, Ghosh S et al (2006) *Mater Char* 57:259–273
- Groeber MA (2007) Ph.D. Thesis, The Ohio State University
- Groeber MA, Ghosh S, Uchic MD, Dimiduk DM (2008) *Acta Materialia* 56:1257-1273

- Groeber MA, Ghosh S, Uchic MD, Dimiduk DM (2008) *Acta Materialia* 56:1274-1287
- Hadwiger H (1957) *Vorlesungen über Inhalt, Oberfläche und Isoperimetrie*, Springer, Berlin
- Han TS, Dawson PR (2005) *Model Sim in Mater Sci Eng* 13:203-223
- Hillert M (1965) *Acta Metall* 13:227-283
- Humphreys FJ (1999) *J. Microscopy* 195:170-185
- Kenney JF, Keeping ES (1947) In: *Mathematics of Statistics*. Van Nostrand
- Kim C-S, Rollett AD, Rohrer GS et al (2006) *Scripta Materialia* 54:1005-1009
- Kral MV, Mangan MA, Spanos G, Rosenberg RO et al (2000) *Mater Char* 45:17-23
- Kammer D, Mendoza R, Voorhees PW et al (2006) *Scripta Materialia* 55:17-22
- Larson B, Yang W, Ice GE et al (2008) *Thin Solid Films*. doi: [10.1016/j.tsf.2008.04.045](https://doi.org/10.1016/j.tsf.2008.04.045)
- Lauridsen EM, Schmidt S, Nielsen SF, Margulies L, Poulsen HF, Juul Jensen D et al (2006) *Scripta Materialia* 55:51-56
- Lewis AC, Bingert JF, Rowenhorst DJ, Gupta A, Geltmacher AB, Spanos G (2006) *Mater Sci and Eng A* 418:11-18
- Lienert U, Almer J, Jakobsen B, Pantleon W, Poulsen HF, Hennessey D, Xiao C, Suter RM et al (2007) *Mater Sci Forum* 539-543:2353-2358
- Li M, Ghosh S, Richmond O, Weiland H, Rouns TN (1999) *Mater Sci Eng A* A265:153-173
- Lorenson and Cline (1987) *Computer Graphics* 21:163-169
- Louat NP (1974) *Acta Metall* 22:721-724
- MacPherson RD, Srolovitz DJ (2007) *Nature* 446:1053
- MacSleyne J, Simmons JP, DeGraef M (2008) *Model Sim Mater Sci Eng*
- Oren PE, Bakke S (2002) *Transport In Porous Media* 46: 311-343
- Oren PE, Bakke S (2003) *J Petroleum Sci And Eng* 39: 177-199
- Przystupa MA (1997) *Scripta Materialia* 37:1701-1707
- Ralph B, Kurzylowksi KJ (1997) *Mater Char* 38:217-227
- Randle V, Hu Y, Rohrer GS, Kim C-S et al (2005) *Mater Sci Tech* 21:1287-1292
- Randle V, Rohrer GS, Hu Y et al (2008) *Scripta Mater*, 58:183-186
- Randle V, Rohrer GS, Miller H, Coleman M, Owen G et al (2008) *Acta Mater* 56:2363-2373
- Rollett AD, Manohar P (2004) In: Raabe D (Ed) *Continuum Scale Simulation of Engineering Materials*, Wiley-VCH, Weinheim, Germany
- Rowenhorst DJ, Gupta A, Feng CR, Spanos G (2006) *Scripta Materialia* 55:11-16
- Russ JC, DeHoff RT (1986) *Practical Stereology*. Springer
- Russ JC (1986) *The Image Processing Handbook*, CRC Press
- Saltykov SA (1958) *Stereometric Metallography*. Metallurgizdat Moscow
- Saylor DM, Fridy J, El-Dasher BS, Jung KY, Rollett AD (2004) *Metall Mater Trans A* 35A:1969-1979

- Saylor DM, El-Dasher BS, Adams BL, Rohrer GS (2004) *Metall Mater Trans* 35A: 1981-1989.
- Saylor DM, El-Dasher BS, Rollett AD, Rohrer GS et al (2004) *Acta Materialia* 52:3649-3655
- Saylor DM, Morawiec A, Cherry KW, Rogan FH, Rohrer GS, Mahadevan S, Casasent D et al (2001) In: Gottstein G and Molodov DA (Eds) *Proceedings of the First Joint International Conference on Grain Growth*, Springer Verlag, Aachen, Germany
- Schmidt S, Nielsen SF, Gundlach C, Margulies L, Huang X, Juul Jensen D et al (2004) *Science* 305:229-232
- Spanos G (2006) *Scripta Materialia* 55:3
- Sundararaghavan V, Zabaras N (2005) *Comp Mater Sci* 32:223-239.
- Talukdar MS, Torsaeter O (2002) *J Petroleum Sci Eng* 33:265-282.
- Talukdar, MS, Torsaeter O, Ioannidis MA (2002) *J Colloid Interface Sci* 248:419-428
- Talukdar MS, Torsaeter, O, Ioannidis, MA, Howard, JJ (2002) *J Petroleum Sci Eng* 35:1-21
- Talukdar MS, Torsaeter, O, Ioannidis, MA, Howard, JJ (2002) *Transport In Porous Media* 48:101-123
- Tewari A, Spowart JE, Gokhale AM, Mishra RS, Miracle DB et al (2006) *Mater Sci Eng A* 428:80-90
- Torquato S (2001) *Random Heterogeneous Materials: Microstructure and Macroscopic Properties*. Springer-Verlag New York
- Underwood E (1970) *Quantitative Stereology*. Addison-Wesley New York.
- Wall MA, Schwartz AJ, Nguyen L (2001) *Ultramicroscopy*, 8:73-83
- Zhang C, Suzuki A, Ishimaru T, Enomoto M et al (2004) *Metall. Trans. A35A*:1927-1932
- Zaafarani N, Raabe D, Singh RN, Zaefferer S et al (2006) *Acta Materialia* 54:1863-1876